CONTENTS

EDITORIAL BOARD

Annual Subscription

Pakistan: Rs 250 Foreign Countries: US$ 40 Overseas Air Mail Charges: US$ 10

**The Journal is published bi-annually
In April and October**

Published by:

Riaz Ahmad for Government College University, Lahore, Pakistan.

Printed at: PRIME Publishers Ltd.

PK ISSN 0022- 2941; CODEN JNSMAC
Vol. 55, (2015) PP 01-11

PRESSURE GRADIENT EFFECTS ON LASER-INDUCED BREAKDOWN SPECTROSCOPY OF Ti PLASMA

A. HAYAT, S. BASHIR*, K. MAHMOOD

Centre for Advanced Studies in Physics, Government College University Lahore, Pakistan.

*E-mail address: shaziabashir@gcu.edu.pk

(Received: 11-05-2016)

ABSTRACT: Laser-induced breakdown spectroscopy (LIBS) of Titanium (Ti) plasma has been investigated under ambient environments of Ar and air for various pressures ranging 10 to 700 torr. Plasma was performed by employing Q- switched Nd:YAG laser pulses ($\lambda \approx$ 1064nm, $\tau\approx$10 nsec, energy of 200mJ). The emission spectra, excitation temperatures, and electron densities are appreciably influenced by the nature and pressure gradients of ambient atmosphere. The maximum line intensity is observed at pressure of 50 torr for Ar atmosphere and at 100 torr for air. Both the electron temperature as well as electron density are found to be increased with increasing pressure up to a certain range of 650 torr and then are decreased. Investigation of the controlled inert gas environment suggests that there exists an optimum pressure range that enhances signal strength of emission lines. Our experimental observations also provide evidence about the formation of a mixing zone between the target plasma and ambient gas that has already been explained on the basis of different hydrodynamical models (Piston model).

Keywords: LIBS, Electron temperature, Electron density, Ambient Pressure.

1. INTRODUCTION

Laser Induced Breakdown Spectroscopy (LIBS) is a rapidly developing and promising technique for plasma diagnostics and material characterization [1-4]. Multi-elemental analysis of solids, liquids and gases with no sample preparation is one of the emerging aspects of this simple technique. However different physical and chemical processes as plasma ignition and plasma decay involved during ablation under ultra high-vacuum, make this technique to be a complex one. Moreover the laser ablation under different ambient conditions suggests additional complexities (formation of shock waves etc). The understanding of plasma dynamics in the presence of different ambient gases becomes significantly important for desired applications e.g. pulsed laser deposition, nano-structuring of materials and LIBS in which the laser ablation is often required to be performed in the presence of background gas [3].

The role of the inert gases in plasma studies (LIBS) has always been appreciated because of its usefulness without perturbing the experimental setup. There are multitudinous experimental confirmations for the Ar gas to be used for best signal strength and for the deprivation of plasma from different undesired chemical reactions. High ionization potential and large atomic mass of Ar are responsible factors for improved thermal insulation and geometrical confinement of plasma [3, 4].

Many hydrodynamic models predict the different mixing phenomena between ambient gas and vapor plume under certain ambient pressures [5, 6]. One of these gas-dynamic models describes the formation of a mixing zone between ambient gas and vapor plume according to which in the presence of an ambient gas, a strong shock wave propagates towards the target to balance an out-coming shock wave. Such inward flux may facilitate the mixing of vapor plume and ambient gas. The width of this zone formed in the periphery of plasma varies depending upon surrounding gas pressure. As the pressure increases up to a certain limit (depending upon the nature of a gas) ambient gas starts to work as a piston which reduces the further mixing of vapor plume and ambient gas [3]. Such effects of background gases have a strong influence on mass ablation rate, the plasma temperature and the electron number density [7-9]. The current work deals with the optimization of Ti plasma evolution using LIBS technique under different ambient gas pressures of Ar and air. The obtained results also verify the hydrodynamic model (Piston model) under the experimental conditions. The fluctuations in intensity profiles of characteristic lines were analyzed as a function of ambient pressure and are significantly contributing plasma characteristic in formation (electron temperature and electron density). The experimental conditions (nature and pressure of ambient t environment) have been optimized for Ti having crucial effects on electron temperature and electron density that in turn are imperative for pulse laser deposition , material processing and structuring.

2. EXPERIMENTATION

A schematic of experimental setup used for LIBS analysis of the material under different ambient pressures is shown in Fig.1. A Q-switched 1064nm Nd:YAG laser (CFR 200 Big Sky laser Technologies Quantel France) delivering pulses at a repetition rate of 1-20 Hz is used as source of plasma formation. The pulse energy was fixed at 200 mJ. The laser beam was focused onto the sample by a 20 cm focal length lens. The targets were placed at a distance of 3cm before the focus in order to suppress ambient breakdown. Samples were mounted on a rotating stage for the analysis of fresh sample surface for each exposure. The optical emission from laser induced Ti plasma was viewed through side window present at 90^0 to the plasma expansion direction.

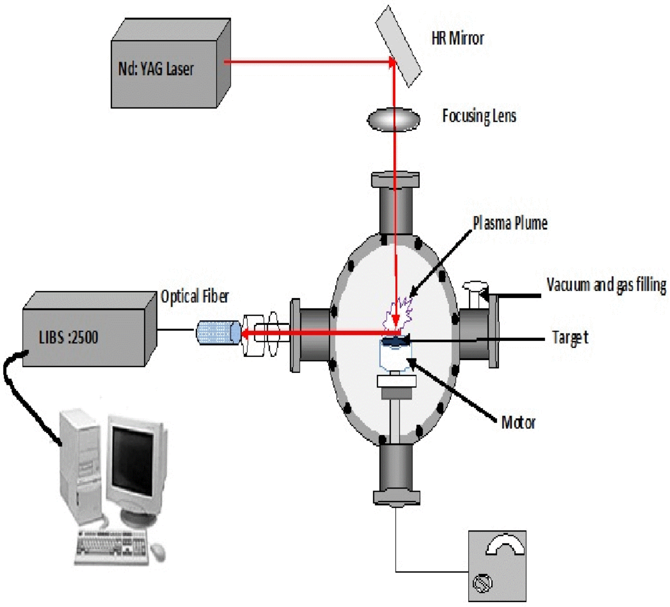

Fig. 1: A Schematic of an experimental set-up.

In order to investigate the effect of nature and pressure dependence of shield gases on the laser-induced breakdown spectroscopy of ablated Ti, the targets were irradiated under different ambient conditions of Ar and air. Plasma was formed in a vacuum chamber, in which the ambient gas pressure could be accurately controlled with a mbar precision. The plasma emission was collected by LIBS2500 plus spectrometer system (Ocean Optics Inc, USA). This system consists of LIBS Fiber bundle with seven linear silicon CCD array detectors for a broadband 200-980 nm analysis, with an optical resolution of 0.1nm. All the measurements have been performed with a time window (integration time) of the order of 2.1 milliseconds. The elapsed time between the arrival of the laser pulse on the sample and the beginning of the measurement (often called delay time) was 1.25 μs. theoretically; this delay is the period of time after the laser vaporizes the material and the spectrometer begins acquiring data.

3. RESULTS AND DISCUSSION

3.1. Emission Intensity Profile:

In the present work, investigations have been performed on spectral response of Ti plasma produced under various ambient conditions. The spectra obtained lie in UV to IR region. The spectral lines Ti (II) 334.67nm, Ti (I) 488.50nm, Ti (I) 551.25nm, Ti (I) 586.64nm, Ti (I) 625.80 nm and Ti (I) 720.94 nm were selected in order to evaluate the excitation temperature and density profiles of Ti plasma.

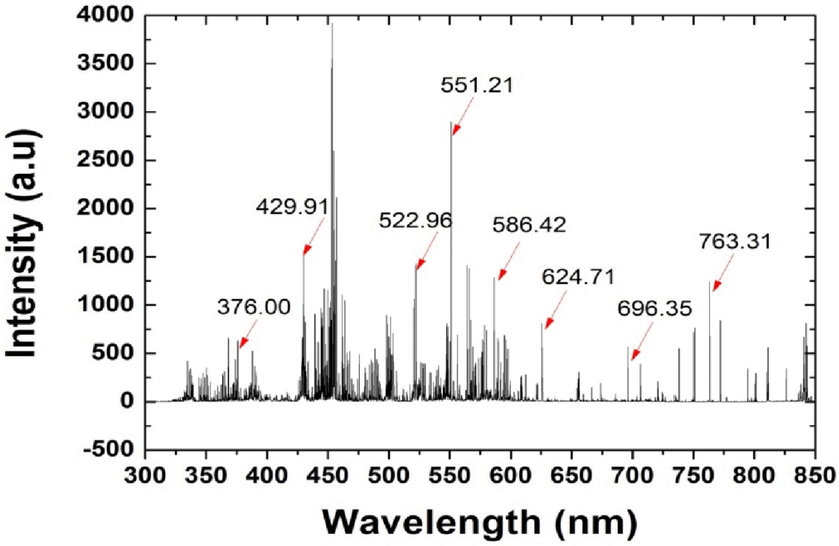

Fig. 2: The emission spectrum of Ti in Ar at a pressure of 10 torr.

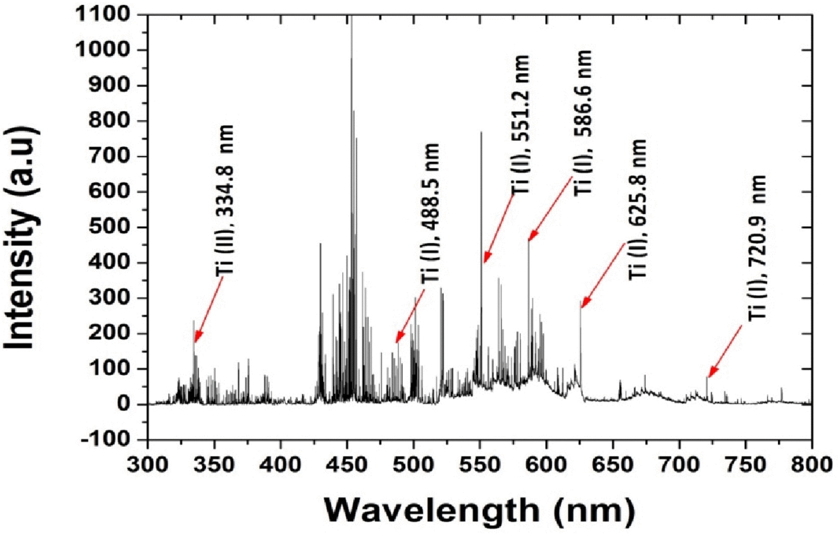

Fig. 3: The emission spectrum of Ti in air at a pressure of 10 torr.

Fig.2 and Fig.3 show the emission spectra of Ti plasma at the pressure of 10 torr for Ar and air atmosphere respectively, consisting of atomic and ionic Ti lines. The spectroscopic parameters of selected transitions used for evaluation of electron temperature and density are listed in table 1 [10, 11].

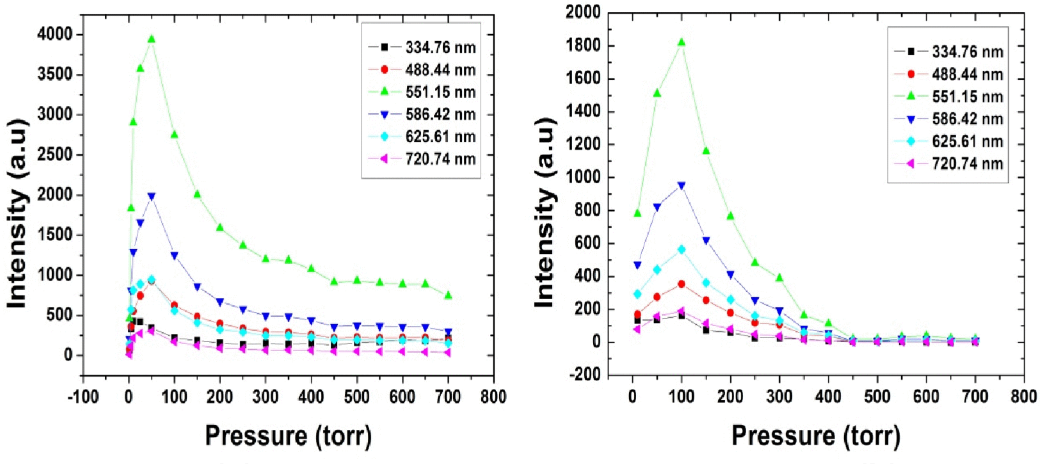

(a) **(b)**

Fig. 4: The intensities of selected wavelengths of Ti plasma at various pressures of (a) Ar and (b) air.

Fig.4 (a, b) shows the comparison of line intensities for selected transitions in Ar and air under different pressures (10-700 torr). The emission intensity profile is different for different ionized lines of Ti. It is observed that initially intensity of all the lines increases with increase in pressure attains its maximum at 50 torr in Ar (Fig.4a) and at100 torr in air (Fig.4b) and then decreases with further increase in pressure. The trend of emission intensity variation for Ti plasma after its ablation in air at the pressure range from10 torr to 700 torr is comparable to that of Ar atmosphere upto a certain extent as there are higher emission intensity values in case of Ar for same transition lines (Fig.4). The emission intensity has maximum value for Ti II 551.25 nm for both air and Ar ambient. This metallic plasma emission intensity profile is in agreement with the previously reported work [12].

The lower emission intensity at pressures less than 50 torr in Ar (100 torr in case of air) is attributed to a reduced shielding effect of the ambient gas plasma due to the lesser gas particle density at reduced pressures. The plasma readily expands into the low-pressure region, decreasing the density of species. This results into reduced absorption of the laser pulse via inverse Bremsstrahlung and less shielding of the target surface. However the nanosecond LIBS plasma studies indicate that using lower surrounding pressure produces plasma expansion in less denser atmosphere that in turn induces less intense shockwave. As more photons will interact together with the target surface due to reduced shock wave density, less intense spectrum will be obtained [13, 14]. The pressure rises upto 50 torr in Ar enhances the collisional frequencies of plasma particles resulting into more momentum transfer and increased cascade growth of electrons [15].

Further increase in pressure 50 torr to 700 torr, there occurs a confinement effect of the plasma nearer to the target surface. This effect shields the target surface. The remaining part of pulse absorbed by the plasma results into a strong shielding and hence reduces the ablated mass from the target [16]. The decrease in LIBS emission intensity with increasing pressure (after 50torr and 100torr) is therefore attributable to plasma shielding i.e. self assimilation of laser energy by plasma itself. The same trend has also been studied in Ar and hydrogen in previous work [17]. At higher pressure peak broadening and self absorption phenomena are prevailed. It is reported that there may be defocusing or misalignment of laser pulse at high pressure resulting in reduced intensity profile. From Fig.4 (a, b) it is clear that the emission intensities are higher in Ar atmosphere than air. This is attributed to thermal characteristics of the ambient gas which are responsible for energy loss from the plasma. The thermal conductivity of the Air (0.0262 W m^{-1} K^{-1}) is larger as compared to the Ar (0.016 W m^{-1} K^{-1}) at 25 ^{0}C. Therefore, the plasma in the air environment cools rapidly as compared to Ar, thus resulting in to low emission intensities [12, 17].

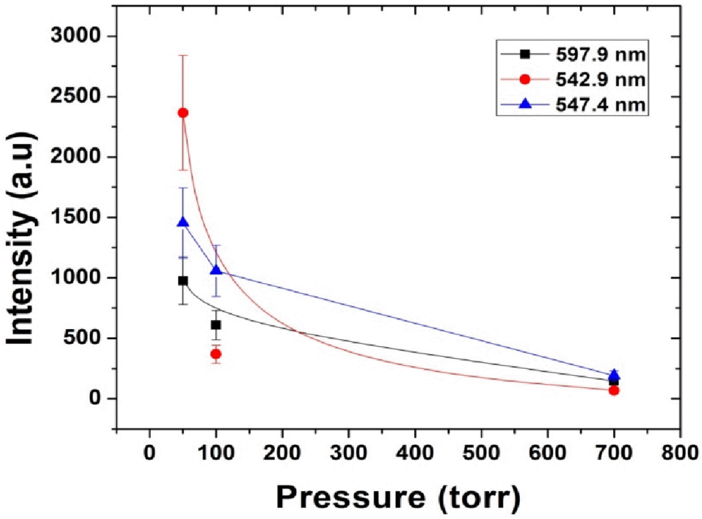

Fig. 5: The pressure versus intensity graph of ionized ambient atoms.

The gas-dynamics model predicts an important mixing effect of argon gas into the vapour plume according to which the conservation and the transformation of the kinetic energy of expanding plume lead this mixing resulting in increase in thermal energy of the argon. The collisions between argon gas and vapour plume, in this mixing zone transfer the energy back and forth. The width of mixing zone that is formed in the periphery of plasma decreases as the ambient pressure increases finally causing the decrease in the intensity of emission lines since the ambient gas starts to act as a piston and reduces further mixing [3]. The obtained emission spectra under different pressures contain ArI, and ArII lines. Fig.5 shows pressure verses intensity plot of ionized ambient atoms so that the aforementioned physical process and hydrodynamic models [4] can be appreciated.

3.2. The Electron Temperature:

In order to understand the different processes within plasma like excitation, dissociation and ionization, the enlightenment about plasma temperature is necessary. Plasma is assumed to be consisting of single electron temperature *(Te)* under local thermal equilibrium condition. This electron temperature can be calculated from obtained spectrum with the help of Boltzmann plot method that can be used for known excitation states. For the evaluation of temperature, emission intensities of six various distinct Ti lines (334.85, 488.50, 551.2, 586.6, 625.8, 720.9 nm)have been selected for Boltzmann plot. Boltzmann distribution is given by the following relation [13].

$$\ln\left(\frac{\lambda_{mn} I_{mn}}{g_m A_{mn}}\right) = -\frac{E_m}{kT_e} + \ln\left(\frac{N(T)}{U(T)}\right) \tag{1}$$

Where I_{mn}, λ_{mn}, A_{mn}, g_m and E_m are the intensity, wavelength, transition probability, statistical weight and energy of upper state m. $U(T)$, $N(T)$, k and T_e are partition function, total number density, Boltzmann constant and electron temperature, respectively. For a given spectrum, a Boltzmann plot of the logarithmic term $\left(\frac{\lambda_{mn} I_{mn}}{g_m A_{mn}}\right)$ versus E_m yields a straight line whose slope is equal to $-1/kT_e$. The calculated value of electron temperature of Ti plasma varies from 7000 K to ~ 9250 K in Ar and 6000 K to 8250 K in air. For different pressures ranges from 10 torr to 700 torr these temperature values have been plotted in Fig. 6. The increasing trend of temperature up to range of 650 torr is observed that decreases with further increase in pressure.

The results show that the temperature values are higher at the higher pressure because of the plume that is confined to a small volume in front of the target. However, the three factors attributed to increase in plasma temperature at higher pressure are the involvement of more ambient molecules in the plasma formation resulting into transfer of laser energy to the material. Second factor is decrease in mean free path of ablated species which increases the collision probability [13]. Third factor is laser supported detonation (LSD) waves where laser pulse deposits some part of its energy to the background gas which is surrounding the plume. Thus during mixing of the ambient gas with plasma plume further energy is transferred to the plasma plume [18]. After 650 torr the decrease in plasma temperature is attributed to shielding effect that becomes dominant for higher pressures.

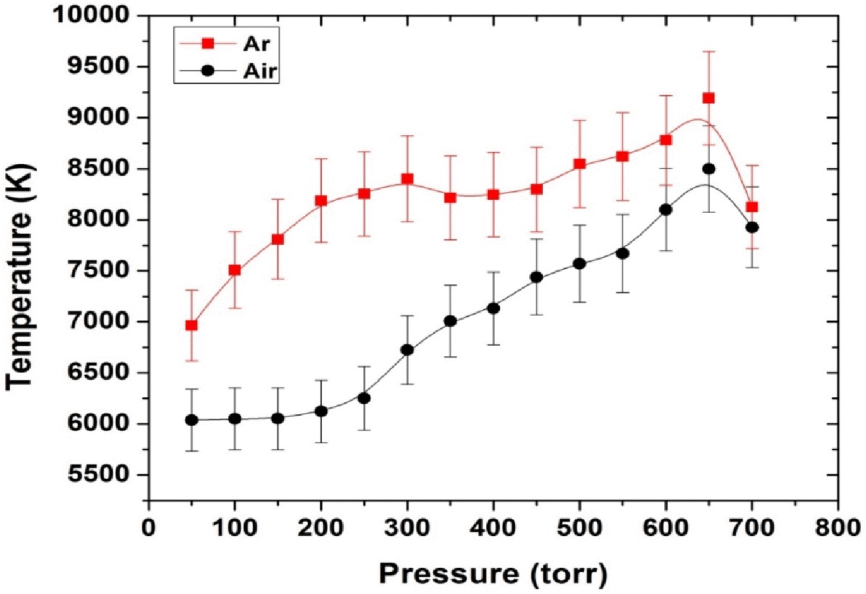

Fig. 6: The variation of electron temperature of Ti plasma as a function of pressure.

The results from LIBS indicate that the values of emission intensity and electron temperature are higher for Ar than for air. Ar as compared to air is a good thermal insulator and has smaller thermal conduction co-efficient. The space-average time cooling rates for Ar and air are about 1×10^{8} Ks^{-1} and 2.3×10^{8} Ks^{-1} respectively. This increase in temperature in the presence of Ar atmosphere is due to negligible heat exchange between plume and ambient gas. While the radiative cooling causes the decrease in temperature where different compressed and ionizes species start to relax [4]. Additionally, the axial length of plasma has a significant influence on plasma temperature and plasma density [12]. This axial length will be smaller for Ar than air (due to higher density of Ar than air) and hence more confined plasma will be formed in the former case resulting in higher electron temperature.

3.3. The Electron Number Density:

By considering local thermal equilibrium (LTE) conditions a Lorentz function is used to evaluate the FWHM of stark broadened lines for the plasma density calculations. The best Lorentzian fit for the line 453 nm having FWHM (≈ 0.0813 ±0.0013) has been used. The stark broadening of emitted lines from plasma occurs due to collisions with charged particles resulting in peak wavelength shift. When the radiating species (atoms or ions) are surrounded by dense plasma, Doppler broadening mechanism is completely negligible in comparison to broadening caused by charged particle (Stark broadening) [11]. This line broadening is important for the determination of electron density. The electron density related to the FWHM of stark broadened line $\Delta\lambda_{1/2}$ nm, is given by the following relation [13, 17].

$$\Delta\lambda_{\frac{1}{2}} = 2w\left(\frac{N_e}{10^{16}}\right) + 3.5A\left(\frac{N_e}{10^{16}}\right)^{\frac{1}{4}}\left[1 - 1.2N_D^{\frac{-1}{3}}\right] \times \omega\left(\frac{N_e}{10^{16}}\right) \qquad (2)$$

Where N_e is the electron number density (cm^{-3}), ω is the electron impact width parameter and A is the ion broadening parameter. Both ω and A are weak functions of temperature and can be interpolated at different temperatures by using quadratic relation [19].

N_D is the number of particles in the Debye sphere and can be calculated by the following relation [1].

$$N_D = 1.72 \times 10^9 \frac{T^{3/2}(eV)}{N_e^{1/2}(cm^{-3})} \qquad (3)$$

The first term in the equation (2) refers to the electron broadening and second term is the contribution from the ion broadening which is very small (in our case) and can be neglected and equation 2 reduces to equation 4 as

$$\Delta\lambda_{\frac{1}{2}} = 2w\left(\frac{N_e}{10^{16}}\right) \qquad (4)$$

The equation (4) is used to calculate electron density where the reference data of [18] is used to get values of ω related to different plasma temperatures.

Fig. 7 is the graph of evaluated electron densities at different pressures. From the data, the maximum evaluated electron density is 9.4×10^{17} cm^{-3} for Ar and 8.9×10^{17} cm^{-3} for air.Our experimental observations reveal that there is increase in electron density with the increase in pressure irrespective of nature of ambient. There are three basic processes responsible for the increase in temperature and electron density as (i) collisions with background gas resulting in excitation (ii) electron impact excitation and (iii) generation of shock waves produced in ambient gas due to plasma expansion which causes the ionization of the gas [17]. It is interesting to remark here

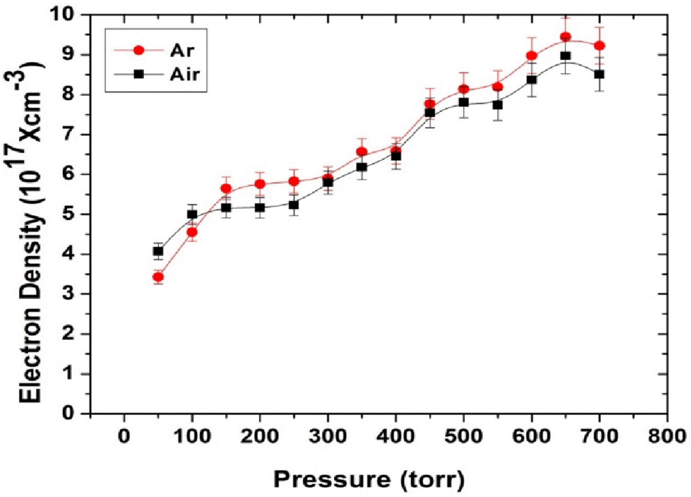

Fig. 7: The variation of electron density of Ti plasma as a function of pressure.

that with the increase in pressure there is manifestation of plasma confinement close to the target surface. This confinement enhances the electron-atom collision frequency which produces more electron concentration. Finally the decrease in plasma temperature and density is due to enhanced shielding effect after 650 torr.

4. CONCLUSIONS

The experimental results reveal that the nature of ambient gas and its pressure is one of the major factor controlling laser induced plasma parameters such as optical emission intensity, electron temperature and density profile. The emission intensity profile has maximum value at pressure of 50 torr for Ar and 100 torr for air and then decreases with further increase in pressure. These results agree with the “piston model” that describes the plasma expansion under high pressure ambient gas environment. A mixing zone is formed at the periphery of plasma due to mingle effect of vapor plume and ambient gas resulting in efficient plasma confinement. The validity of this model is supported by measuring the intensity values of ionized ambient atoms at different pressures that exhibit the decreasing trend with increase in pressure. The increasing trend of plasma temperature and plasma density upto a certain value is attributable to confinement effects and finally decreases due to the shielding effect.

ACKNOWLEDGMENT

We are thankful to higher education commission of Pakistan for funding the project “Upgradation of Laser facilities at CASP, GC University, and Lahore” and Director CASP for providing facilities.

REFERENCES

1. L. J. Radziemski and D. Cremers, Handbook of Laser-Induced Breakdown Spectroscopy, John Wiley and Sons, England, (2006).
2. S. Bashir, N. Farid, K. Mahmood and M. S. Rafique, Appl. Phys. A, 107 (2012) 203.
3. Q. L. Ma, V. Motto-Ros, W. Q. Lei, M. Boueri, L. J. Zheng, H. P. Zeng, M. Bar-Matthews, A. Ayalon, G. Panczer and J. Yu, Spectrochim. Acta B, 65 (2010) 707.
4. E. Tognoni, V. Palleschi, M. Corsi and G. Cristoforetti, Spectrochim. Acta B, 57 (2002) 1115.
5. N. Arnold, J. Gruber and J. Heitz, Appl. Phys. A: Mater. Sci. Pro., 69 (1999) 587.
6. S. Wen, X. Mao, R. Grief and E. Richard, J. Appl. Phys., 101 (2007) 023115.
7. G. Cristoforetti, S. Legnaioli, V. Palleschi, A. Salvetti and E. Tognoni, Spectrochim. Acta B, 59 (2004) 1907.
8. A. A. I. Khalil, Laser Phys., 20 (2010) 238.
9. S. H. G. Asimellis, A. Giannoudakos and M. Kompitsas, Spectrochim. Acta B, 60 (2005) 1132.
10. Moore C E, Atomic Energy Levels, NBS Circular No. 467, US Govt Printing Office, Washington DC, (1971).
11. W. L. Wiese and J. R. Fuhr, J. Phys. Chem., Ref. Data 4, (1975) 263.
12. S. S. Harilal, C. V. Bindhu, V. P. N. Nampoori and C. P. G. Vallabhan, Appl. Phys. Lett., 72 (1998) 167.
13. R. Shu, H. Qi, G. Lv, D. Ma, Z. He and Y. Xue, Chin. Opt. Lett., 5 (2007) 58.
14. N. Farid, S. Bashir and K. Mahmood, Phys. Scr., 85 (2012) 015702.
15. N. M. Shaikh, S. Hafeez, S. Mahmood, M. Saleem and M. A. Baig, J. Appl. Phys., 100 (2006) 073102.
16. P. T. Rumsby and J. W. M. Paul, Plasma Phys., 16 (1974) 247.
17. N. M. Shaikh and M.A. Baig, Spectrochim. Acta B, 62 (2007) 1311.
18. J. A. Aguilera, C. Aragón, G. Cristoforetti and E. Tognoni, Spectrochim. Acta B, 64 (2009) 685.
19. X. Zeng, X. Mao, S. S. Mao, J. H. Yoo, R. Grief and R. E. Russo, J. Appl. Phys., 95 (2004) 816.

PK ISSN 0022- 2941; CODEN JNSMAC
Vol. 55, (2015) PP 13-17

A NOTE ON CONTROLLABILITY AND OBSERVABILITY OF A MATHEMATICAL MODEL FOR DIABETES MELLITUS

R. HUSSAIN*, A. ALI, R. SHAHZADI

Mirpur University of Science and Technology (MUST), Mirpur AK, Pakistan.

*E-mail address: rashida12@gmail.com

(Received: 24-02-2016)

ABSTRACT: This paper is about the controllability and observability of mathematical model for glucose insulin regulatory system of diabetes mellitus. We analyzed the model proposed by Sandhya and Deepak Kumar [1]. The model comprised of three equations with 8 parameters. It was nonlinear model. So we linearized it about equilibrium points. Then property of controllability and observability were examined by taking insulin as input and glucose as output. The result presented is that, the model is controllable but not observable.

Keywords: Diabetes mellitus, Mathematical model, Controllability, Observability.

1. INTRODUCTION

Diabetes mellitus or simply diabetes is a disorder of metabolism. It is a disease in which a person has high or low sugar level. Diabetes may occur due to two defects. These defects are either due to no insulin production by pancreatic beta cells or no response of insulin by body cells. Combinatorial effects of genetics, environment and immunological factors lead the destruction of beta cells [2]. Insulin is an enzymatic protein, which is composed of 51 amino acids. Insulin is produced by beta cells of the pancreas (a body organ). The blood glucose level is regulated by insulin.

Two main types of diabetes are proposed by WHO (World Health Organization) committee in 1980. They classified the types by giving their name as IDDM (Insulin Dependent Diabetes Mellitus) or Type 1 and NIDDM (Non Insulin Dependent Diabetes Mellitus) or Type 2. In 1985 IDDM and NIDDM were considered as names for types of diabetes [3].

Type 1 is chronic conditional diabetes in which pancreas produces little or no insulin. In this type of diabetes body immune system attacks and destroys the beta cells. This means that the body can no longer produce and secrete insulin into the blood and regulate the blood glucose concentration. This attack is called autoimmune disease. Type 1 comprised of 12 to 15 percent of cases of diabetes [4]. Type 2 is also a chronic condition. It affects the way in which our body metabolizes the sugar. The body resists the insulin in diabetes of Type 2. Type 2 diabetes mellitus is mainly characterized by two defects which are impure insulin secretion and insulin resistance [5]. Recently a steady demographic shift of type 2 in the younger population is noted.

As high blood glucose and low blood glucose level are very crucial to a person's health. Without monitoring the blood glucose level a person gets metabolic illness which can damage his health. Diabetes mellitus can damage organs like heart, kidney and pancreas. Sandhya and Deepak Kumar proposed a mathematical model for diabetic patients. This model is for glucose, insulin regulatory system of diabetes mellitus. Many models were already developed for diabetes, but those models are valid for certain specific conditions. Deepak Sandhya's model is a very simple model and is valid in all conditions of diabetes.

For this model, the data of many patients were collected. But in the present work we take the data of one patient. Controllability and observability of model has been checked by using this data.

2. MATHEMATICAL MODEL

Consider a mathematical model with three factors; Insulin sensitivity, glucose effectiveness, and pancreatic responsiveness, referred to in Pacini and Bergman [6], play an important role in glucose disposal.

These factors are shown by variables like *G, X* and *I*. *G* shows the glucose level, *X* shows glucose uptake activity and *I* show the insulin level in diabetic patient. This model has many parameters whose Basel values are also involved like G_b and I_b. So the equations of the model are defined by [1].

$$\frac{dG}{dt} = -m_1 G + m_2 I + m_1 G_b \, , \tag{1}$$

$$\frac{dX}{dt} = -m_2 X + m_3 I - m_3 I_b + m_6 I_b \, , \tag{2}$$

$$\frac{dI}{dt} = -m_3 I + m_4 G + m_4 m_5 - m_6 I + m_6 I_b \, , \tag{3}$$

Where *G(t)*is the plasma glucose concentration at time *t*$\left(\frac{mg}{dl}\right)$, *X(t)* is the generalized insulin variable for the remote compartment (min^{-1}), *I(t)* is the plasma insulin concentration at time *t*$\left(\frac{\mu U}{ml}\right)$, G_b is the Basal pre-injection value of plasma glucose $\left(\frac{mg}{dl}\right)$, I_b is the Basal pre-injection value of plasma insulin $\left(\frac{mg}{dl}\right)$, m_1 is insulinindependent rate constant of glucose rate uptake in muscles, liver and adipose tissue (min^{-1}), m_2 is the rate of decrease in tissue glucose uptake ability (min^{-1}), m_3 is the insulin independent increase in glucose uptake ability in tissue per unit of insulin concentration $I_b\left(min^{-2}\left(\frac{\mu U}{ml}\right)\right)$, m_4 is the rate of the pancreatic beta cells release of insulin after the glucose injection and with glucose concentration above *h*$\left(\left(\frac{\mu U}{ml}\right)(\,min^{-2})\,\left(\frac{mg^{-1}}{dl}\right)\right)$, m_5 is the threshold value of glucose above which the pancreatic beta cells release insulin, m_6 is the first order decay rate of insulin in plasma (min^{-1}) pancreatic beta cells release insulin.

3. CONTROLLABILITY AND OBSERVABILITY FOR NORMAL PERSON

3.1 Values of Parameters:

The associated table shows the values of parameters involved in equations (1)-(3). We consider the values of parameters for normal person [1].

Table 1:

Parameters	G_b	I_b	m_1	m_2	m_3	m_4	m_5	m_6
Values	80	7	0.0317	0.0123	0.0000049	0.0039	79.035	0.2659

3.2 Model after Parameter Substitution:

By substituting the values of parameters from Table 1, we get:

$$\frac{dG}{dt} = -0.0317\,G + 0.0123\,I + 2.53600\ , \qquad (4)$$

$$\frac{dX}{dt} = -0.0317\,G + 0.0123\,I + 1.8612\ , \qquad (5)$$

$$\frac{\mathrm{dI}}{\mathrm{dt}} = -0.2569\ \mathrm{I} + 0.0039\ \mathrm{G} + 2.1695\ . \qquad (6)$$

3.3 Equilibrium Points:

We get 83.65, 9.415, and 151.32 as equilibrium points by putting left hand side of equations (4)-(6) equal to zero.

3.4. Linearized Equations:

The Linearized equations about equilibrium points are

$$\frac{\mathrm{dG}}{\mathrm{dt}} = -0.0317\,\mathrm{G} + 0.0123\,\mathrm{I}\,, \qquad (7)$$

$$\frac{\mathrm{dX}}{\mathrm{dt}} = -0.0317\,\mathrm{G} + 0.0123\,\mathrm{I}\ \ , \qquad (8)$$

$$\frac{dI}{dt} = -0.2569\,I + 0.0039\,G\ . \qquad (9)$$

3.5 Linear Control:

The linear control system is defined by

$$\frac{dX}{dt} = A\,x(t) + B\,u(t), \qquad y = Cx(t),$$

Where *x(t)* ∈ R^n, *u(t)*∈ R^p and *y(t)* ∈ $R^k$for t∈ *I*. *A(t), B(t)* and *C(t)* be matrices in L^2 (*I,R*), defined on *I* and have appropriate dimensions i.e., *A(t)* is *n* by *n*, *B(t)*is *n* by *p* and *C (t)* is *k* by *n* matrix. *I* = $[\mathrm{t}_0\ ,\mathrm{t}_\mathrm{e}]$, $t_0 < t_e < \infty$ respectively *I*= t_0,∞).

In this case we have a matrix *X* of the form:

$$X = [\mathrm{G} \quad \mathrm{X} \quad \mathrm{I}]^{\mathrm{T}},$$

by substituting the values from linearized equations, we get:

$$A = \begin{bmatrix} -0.0317 & 0 & 0.0123 \\ 0 & -0.0123 & 0.0000049 \\ 0.0037 & 0 & -0.2657 \end{bmatrix}$$

3.6 Input and Output Matrices:

Let us take insulin as only input and glucose as output. So we have Bas input matrix and Cas output matrix. Then

$$B= [0 \quad 0 \quad 1]^{T} \text{ and } \quad C= [1 \quad 0 \quad 0].$$

3.7 Controllability and Observability Matrices:

The controllability matrix R and observability matrix Q will be defined as:

$$R= [A \quad AB \quad A^2B] \text{and Q} = [C \quad CA \quad CA^2]^{T}$$

3.8. Analysis of Controllability and Observability:

By finding the rank of matrix *R* and matrix Q, we get

Rank (*R*) = 3 and Rank (*Q*) = 2.

Hence our system is controllable because matrix *R* has full rank. But our system is not observable because Q has not full rank.

4. STABILITY OF THE MODEL

To check the stability of model, we have found the eigenvalues by using matrix *A*. The eigenvalues are -0.0231, -0.0123, -0.0257.

Since all the eigenvalues are negative, so our model is locally asymptotically stable. We have plotted the graph of equation (7) and (9), i.e., between glucose and insulin.

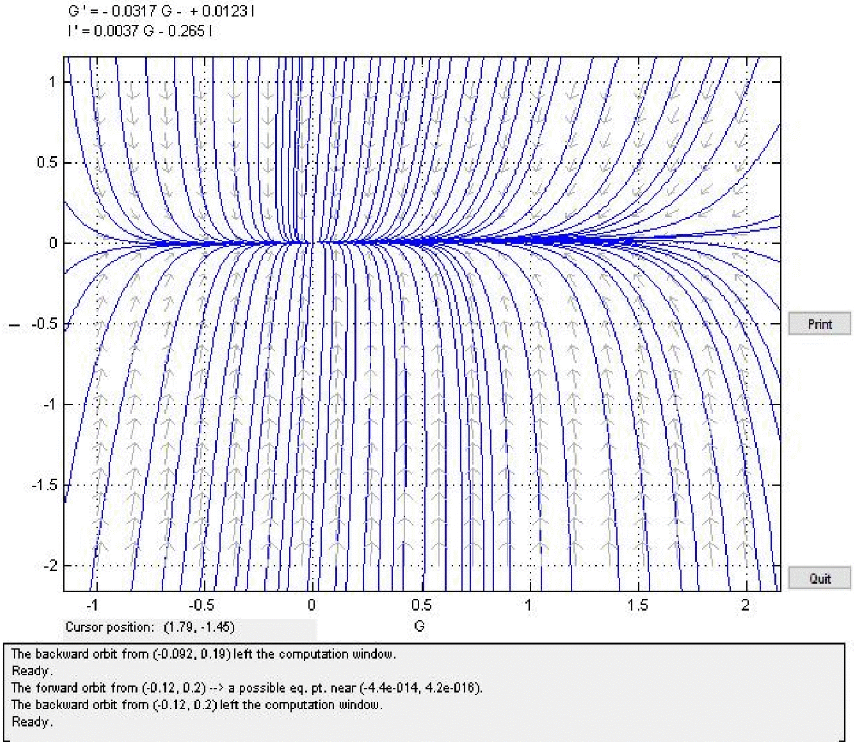

```
Cursor position:  (1.79, -1.45)
```

```
The backward orbit from (-0.092, 0.19) left the computation window.
Ready.
The forward orbit from (-0.12, 0.2) --> a possible eq. pt. near (-4.4e-014, 4.2e-016).
The backward orbit from (-0.12, 0.2) left the computation window.
Ready.
```

Fig.1: Stability of G and I for Normal person

5. CONCLUSIONS

In this paper, we have discussed the two control properties of Sandhya and Deepak Kumar's model after linearizing the model about equilibrium points. The model is controllable but not observable. This result shows that it is not possible to design a stabilized feedback control system by taking insulin as input and glucose as output. This model is not observable in the case of a normal person. So we cannot apply it in the case of diabetic patient. Hence we can say that this model will not be helpful in the development of an artificial pancreas. It requires some improvements. Hence, in future, there is need to develop a comprehensive Deepak Sandhya's model to control a mechanism of the system by adding some other parameters for controllable input and observable output.

REFERENCES

1. Sandhya and D. Kumar, Advances in Applied Mathematical Biosciences, 2 (2011) 39.
2. E. Ahmadi, Z. Rahnama, and A. R. Tehrani, American Journal of Immunology, 5 (2009) 98.
3. W. Sarah, R. Gojka, G. Anders, S. Richard and K. Hilary, Diabetes Care, 27 (5) (2009) 1047.
4. M. Smith, D. Hopkins, R. Peveler, R. I. G. Holt, M. Woodward, and K. Ismail, The British Journal of Psychiatry, 192 (2008) 406.
5. M. A. Ganie and S. Kotwal, Continuing Education for General Practitioners, 25 (3) (2012) 171.
6. G. Pacini and R. Bergman, Computer Methods and Programs in Biomedicine, 23 (2) (1986) 113.

PK ISSN 0022- 2941; CODEN JNSMAC
Vol. 55, (2015) PP 19-33

ROLE OF ION IRRADIATION PROCESS ON THE STRUCTURAL AND ELECTRICAL PROPERTIES OF WN FILMS SYNTHESIZED BY PLASMA FOCUS DEVICE

A. HUSSNAIN*[1], H. M. SIDDIQUE[1], T. HUSSAIN[2], J. SIDDIQUI[2]

[1]Department of Physics, GC University, Lahore 54000, Pakistan

[2]Centre for Advanced Studies in Physics, GC University Lahore 54000, Pakistan.

*E-mail address: ah.shah14@gmail.com

(Received: 17-05-2016)

ABSTRACT: Tungsten nitride films are synthesized on Si substrates at room temperature for different focus shots ion irradiation process. The surface properties of the exposed substrate against various (5, 10, 15 and 20) focus shots are investigated for structure, surface morphology and surface resistivity of synthesized WN films, using X-ray diffraction (XRD), scanning electron microscope (SEM), atomic force microscope (AFM) and four point probe. XRD spectra of exposed substrate show the presences of different phases of tungsten nitride compounds along with some peaks of silicon nitride peaks. The crystalline phases and stresses present in the deposited WN films are strongly depended on the number of focus shots. Crystallite size increases with the increase in the number of focus shots. The SEM micrographs show the strong effect of heating and subsequently melting/quenching effect on the deposited WN films. Voids and cracks in the surface of deposit films are clearly seen in all number of focus shots. The roughness of the exposed substrate is investigated by AFM. It increases with the increase in the number of focus shots and maximum roughness (~60 nm) is measured at 20 focus shots. The resistivity of the substrate surface reduces with the increase in the number of focus shots and lowest resistivity (2×10^{-3} ohm/square) is observed for 20 focus shots.

Keywords: Tungsten nitride, Plasma focus, Four point probe, Silicon wafer, Surface roughness.

1. INTRODUCTION

Transition Metal Nitrides (TMNs) are very attractive due to their fascinating properties like chemical stability, high hardness and good wear resistant endorsed to employ it as hard coatings on cutting tools, turbine blades, engine parts in automobile industry [1-4] and diffusion barriers at elevated temperature in microelectronics devices [5-8] which can also be employed as electrodes for field effect transistors (FET) and thin film capacitors. Different techniques have been used for the synthesis/deposition of tungsten nitride films such as pulsed laser ablation (PLD) [9], cathodic arc [2], chemical vapour deposition (CVD), plasma focus [10], [6] and DC/RF sputtering [11] etc. Plasma focus has been employed for plasma processing of various material surfaces [12-14].

Plasma focus (PF) system is a pulsed plasma device that produces hot (1-2 keV), dense ($10^{25\text{-}26}$ m^{-3}) plasmoid for a short duration (~0.1 μSec). This hot dense plasmoid produces energetic ions, relativistic electrons, X-rays and neutrons [15]. The energetic ions/electrons emitted from this short-lived plasmoid have been engaged in plasma processing of materials such as thin film deposition [16, 17], surface modification [18], ions implantation [19], and thermal surface treatment [20]. Thin films deposition under reactive background with better deposition rate on the substrate at room temperature is highly desirable. Plasma focus system is a possible competitor for these necessities.

The bombardment of energetic ions and formation of new compounds can change surface properties of the material under consideration. So in present research work, we studied the structural, surface morphological/topographical and electrical properties of synthesized tungsten nitride WN films at room temperature with different number of focus shots.

2. EXPERIMENTAL DETAIL

Tungsten nitride thin films are synthesized on silicon (Si) substrate at room temperature using electron/ion beams emerges from Mather-type (3.2 kJ) plasma focus system. The systematic diagram of Mather-type plasma focus system is shown in figure 1. Electrode system hosted in a stainless steel chamber is energized by a single Maxwell fast discharging capacitor (32 μF, 14 kV) with maximum energy up to 3.2 kJ. Details/specifications of the electrode system of plasma focus can be found elsewhere [21-23]. The chamber is evacuated down to a pressure of 10^{-2} mbar by using rotary van pump than nitrogen gas is filled in the chamber up to 2 mbar pressure (optimum pressure). The focusing of every single shot is monitored on oscilloscope attached with Rogowski coil and high-voltage (HV) probe. A typical signal of HV probe is given in figure 2. The very first peak appeared in the HV signal is due to the discharging of the capacitor while second peak indicates the focusing status. A sharp peak indicates best focusing while no/low intensity peaks indicate the weak focusing. Few early weakly focused shots are avoided to affect the substrate by placing a shutter in front of the substrate. Tungsten insert is placed at anode tip that completely covers the copper anode to reduce the deposition of copper impurities onto the substrate material. Si-substrates are cleaned with acetone and then with distilled water for 20 mints each in an ultrasonic bath. Si-substrate is mounted on a sample holder and placed substrate along the Anode axis at 10 cm from Anode tip. The Si-substrate was exposed against various (5, 10, 15 and 20) numbers of focus shots.

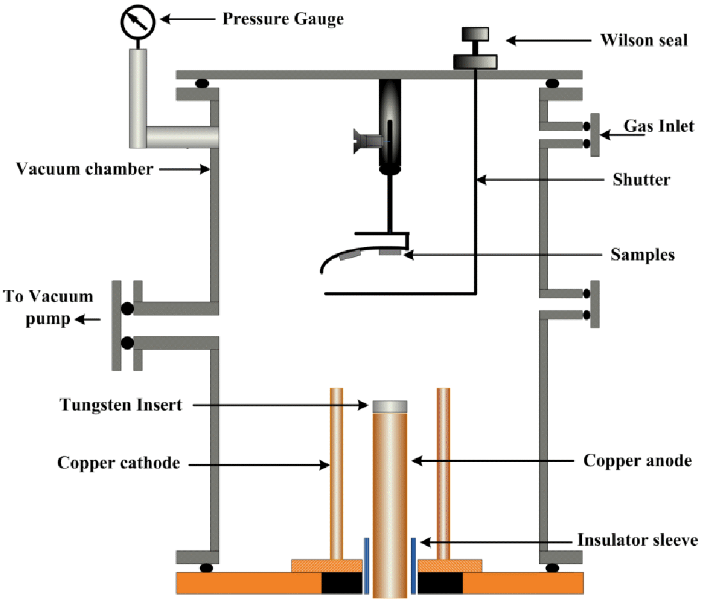

Fig. 1: Schematic diagram of Mather-type Plasma Focus

The structural properties of synthesized coatings are characterized by using X'PERT PRO PANalytical X-ray diffractometer operated at 40 kV, 40 mA in θ-2θ scan mode with radiation CuKα (λ = 1.54Å). The surface morphology of exposed surface is investigated by scanning electron microscope (HITACHI S-3400N) operated at 5 kV and Topography of the exposed surface was examined by atomic force microscope (SPM 9500J). The resistivity of the synthesized coatings is determined by four-point probe.

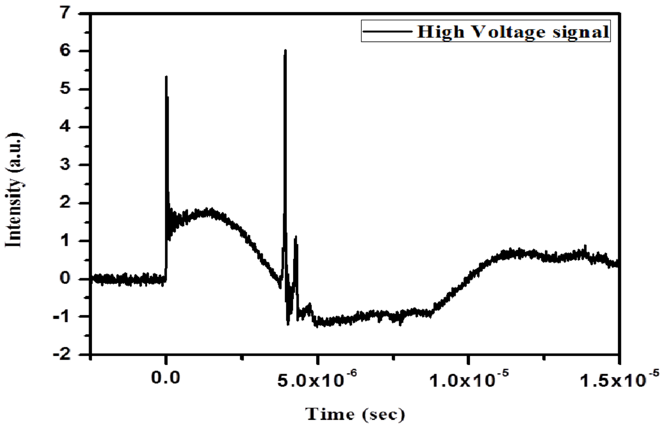

Fig. 2: A typical signal of high voltage probe

3. RESULTS AND DISCUSSION

3.1. XRD Analysis

Figure 3. represents the XRD patterns of WN films synthesized on Si substrate for different (5, 10, 15 and 20) focus shots while the substrates are placed along anode axis at 10 cm in front of anode tip. All the XRD peaks concerning to different phases of WN_2, W_5N_4 and Si_3N_4 are in reasonable agreement with the Inorganic Crystal Structure database (ICSD) reference code [01-083-1287, 03-065-4761, 01-075-0998].

The XRD patterns consist of different phases of tungsten nitride (WN_2, W_5N_4) and silicon nitride (Si_3N_4) compounds, confirming the deposition of composite films on Si-substrate. XRD spectra show that all the deposited films are polycrystalline and the peak intensity of these phases, changes with the change in number of focus shots. By increasing the focus shots, the crystallite size of all phases increases as more ions are incorporated. No new phase is found for 5 number of focus shots, which indicates that 5 number of focus shots are not enough to start the nucleation for the formation of crystalline tungsten nitride or it may be present in the substrate surface in its amorphous form [24].

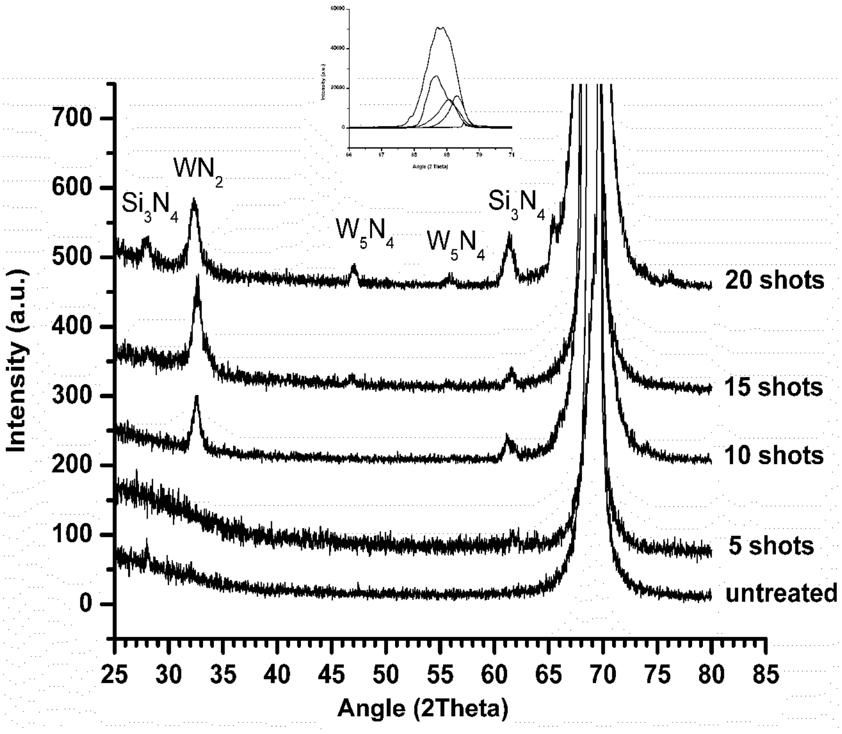

Fig. 3: XRD patterns of deposited WN films for different number of shots.

The diffraction peak corresponding to WN_2 (006) plane reflection having d-spacing of 2.73Å is observed for 10, 15 and 20 numbers of focus shots. The XRD spectra for Si-substrate treated with 20 focus shots show additional peaks at 2θ positions of 47° and 55.84° with the corresponding d-spacing of 1.9318Å and 1.6465Å, which are identified for (105) and (107) planes of W_5N_4 phase. The peak corresponding to silicon nitride is also found for 5, 10, 15 and 20 focus shots. Different tungsten nitride phases confirmed by XRD spectra are WN_2 and W_5N_4 which has rhombohedral and hexagonal structure. This specifies the deposition of stoichiometric tungsten nitride thin films. The XRD spectra show that peak intensity of phases increases at higher focus shots which suggesting the increase in the crystallite size of respective phases. This is may be due to the increase in the thickness of deposited WN films which increases by increasing ion dose that increases by increasing the number of focus shots.

The crystallinity of the films enhances with the increase in the thickness of films. The high energy ion flux plays an important role in the growth of as-deposited crystalline tungsten nitride thin films. The diffraction peaks corresponding to (115) and (321) planes of silicon nitride multiphase are also observed on Si-substrate exposed with 5, 10, 15 and 20 focus shots. Polycrystalline films containing WN and SiN phases are deposited on Si substrate. While monocrystalline silicon transformed into polycrystalline silicon due to ion irradiation by plasma focus. The formation of polycrystalline silicon domains may be attributed to fast energy deliverance by the ion beam which can cause self-annealing of some of the amorphous regions. During the implantation, the strong thermal effect causes the fast temperature rise of the substrate surface, that results in strong temperature gradients from the surface to the bulk of the substrate followed by the fast cooling (in few tens of microseconds) [25]. The small shifting in the diverse peaks from their related stress free data show the presence of residual stress in the composite films which is caused by ion implantation, thermal shocks in addition to grain refinement. The silver colour of deposited films on Si-substrate indicates the synthesis of tungsten nitride thin films on substrate surface. Furthermore, the formation of different compounds of tungsten nitrides confirms the ablation of tungsten material from the W-insert placed at anode tip. The ablation of tungsten material from anode is due to the bombardment of relativistic electrons emerged from the focus column. Ablated tungsten material may interact with the nitrogenous ions and form various tungsten nitride phases and deposited on the Si-substrate surface. It is also possible that all the ablated tungsten plasma may not interact with nitrogen ions and may be deposited on the substrate as tungsten atoms. While the energetic ions coming from next focus shots may sputter the previously deposited films and recombine with the next bunch of ions of same focus shots [26] forming tungsten nitride phase and re-depositing onto the Si-substrate. These energetic nitrogen ions may also cause nitriding of previously deposited films hence increasing the nitrogen content in deposited films.

Crystallite size of the different planes observed in the XRD spectra is estimated by using Debye Scherrer's formula [27].

$$4. \quad Crystallite\ size = \frac{k\lambda}{FWHM\ cos\theta}$$

Where 'k' is a Scherrer's constant with values 0.9 to 1, here 'k' is about 0.93 and 'β' is full width at half maximum of the respective profile in radians, 'λ' is wavelength of incident beam with a value of 1.5406 Å and 'θ' is the Bragg's angle. Figure 4. shows the crystallite size of different phases as a function of focus shots. The estimated values of crystallite size of WN_2 (006) plane for (10, 15 and 20) focus shots are found to be ~11 nm, ~15 nm and ~21 and ~16 nm, ~18 nm and ~25 nm for Si_3N_4 (321) plane respectively.

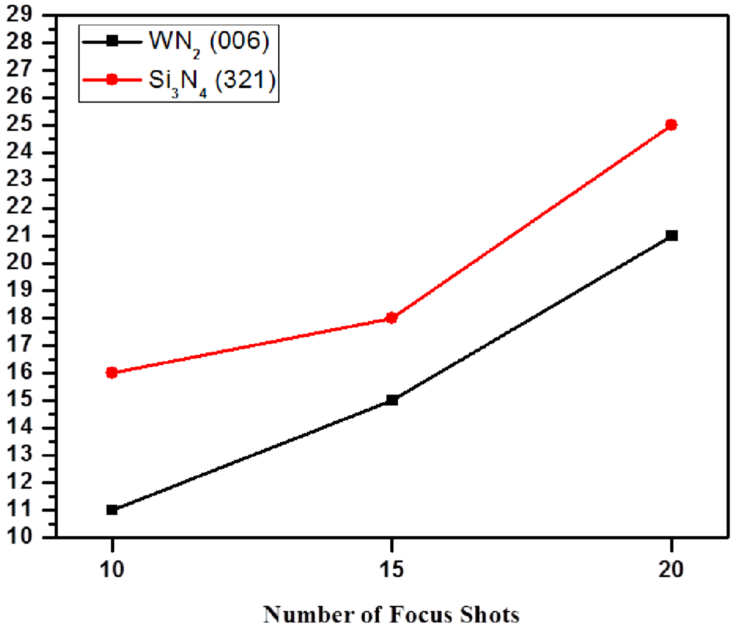

Fig. 4: Variation in crystallite size of WN_2 and Si_3N_4 as a function of various focus shots

Crystallite size of both planes increases by increasing the focus shots as peak intensity of these phase increases at higher number of focus shots. Crystallite size depends strongly on different parameters such as crystal defects and micro-strain effects, thermal shocks, d-values and surface transient temperature which are developed during the deposition process.

3.2. SEM Micrographs:

The surface morphology of the exposed substrate was observed by Scanning Electron Microscope. Figure 5. shows the surface morphology of substrates exposed for 5, 10, 15 and 20 deposition shots when the samples are placed at 10 cm along anode axis.

The surface morphology of the exposed substrate for 5 deposition shots shows some wavy like structures along with some cracks on the surface. Some pits and voids can also be clearly seen in the deposited thin film, however, no specific grains or particles are observed, however, surface of exposed substrate is very smooth with wavy like patterns which are distributed over the whole surface. Wavy like structures arises on the surface of the substrate exposed for 5 focus shots due to the rise in the surface temperature which is caused by the bombardment of highly energetic ions emerges from plasma column. The energetic ions interacting with substrate rises the substrate bulk temperature which leads to the melting and then quenching [28, 29] which develops the cracks on the substrate surface.

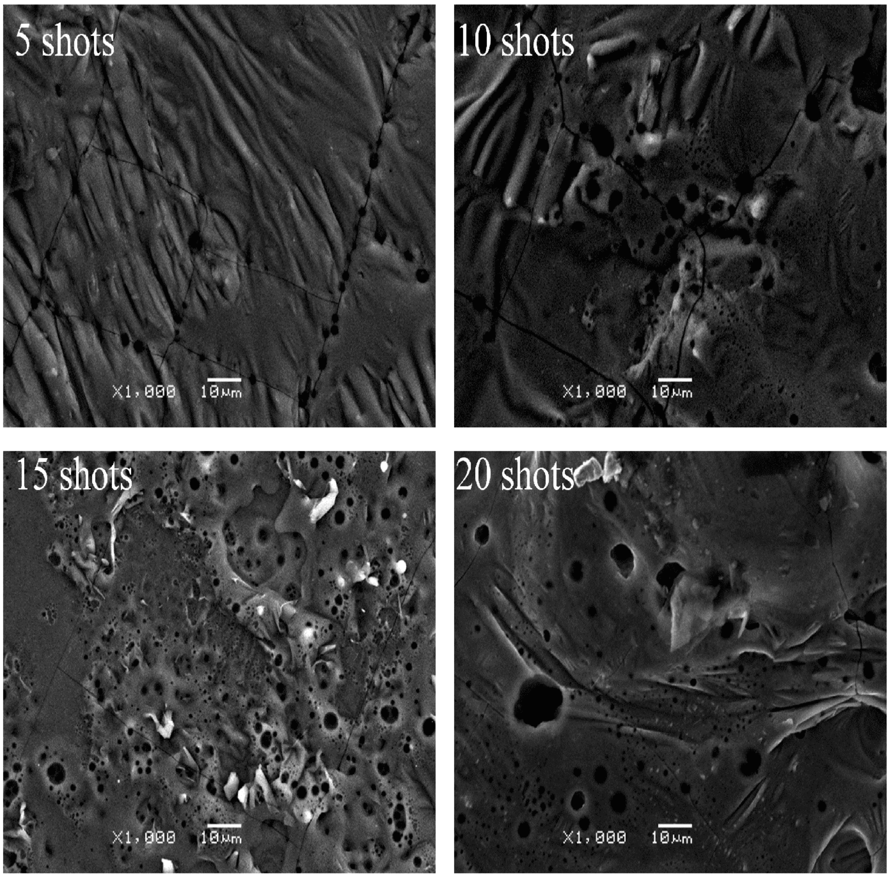

Fig. 5: SEM micrographs of exposed substrate against various focus shots

SEM micrograph of exposed substrate for 10 focus shots shows the increase in the size of wavy like structures while the size of voids and pits is also increased. Surface morphology shows the widening of cracks at higher number of focus shot, while melting is clearly observed at the substrate surface without any distinct structure of grains or particles. At 15 focus shots, more melting on the surface of deposited thin film is observed along with the increase in the numbers and size of pits/voids. The surface morphology of the deposited film shows the presences of some cracks. As the undesirable process of rapid melting followed by subsequent cooling causes brittleness of the samples which is incident by the graduate emergence of micro cracks on the surface of the thin films. The uneven surface suggests that the surface roughness of the deposited films is increased. The SEM micrograph of exposed substrate at 20 focus shots shows large voids/pits on the surface along with few crakes. Melting effect is also clearly visible in the surface along with uneven surface morphology. Some small granular structures are also visible in the micrograph. The increase in the melting effect along with uneven surface is responsible for increasing the surface roughness.

3.3. Atomic Force Microscopy Results:

The surface topography of tungsten nitride thin film is examined by Atomic Force Microscope. Figure 6. Shows the 2D & 3D topography of the substrate exposed for 5, 10, 15 and 20 focus shots along with unexposed Si-substrate. Figure 7 shows the root mean square (RMS) roughness of substrates. The unexposed Si-substrate shows clear the surface with few bright spots which may be due to some impurity on the surface. The surface topography of exposed substrate against 5 focus shots shows almost smooth surface with closely packed tungsten nitride particles. While at 10 focus shots the density of particles increases which increases the surface roughness. The surface topography of the films deposited for 15 and 20 focus shots shows that the size of the closely packed particles increases. The surface roughness increases at 15 and 20 focus shots which are evident by the uneven surface of exposed substrate at higher number of focus shots. The surface topography of all the substrate samples shows almost rough surface composed of closely packed tungsten nitride particles of different sizes.

RMS roughness is an important parameter which is extensively being used for the thin film characterization which is estimated by using the relation.

$$R_{rms} = \sqrt{\sum_{n=1}^{N} \frac{\left(Z_n - \bar{Z}\right)^2}{N}}$$

Where Z_n is the measured height of the *n*-th point in the scan area, Z is the average of height and N is the number of height measurement. RMS of the tungsten nitride thin film prepared for multiple focus shots is given in figure 7.

Untreated

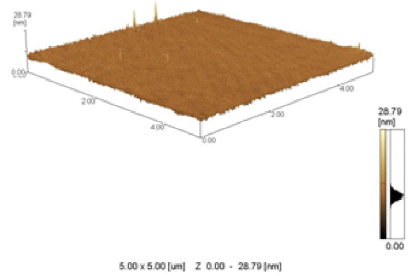

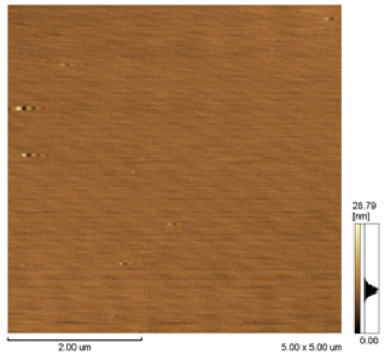

5 Shots

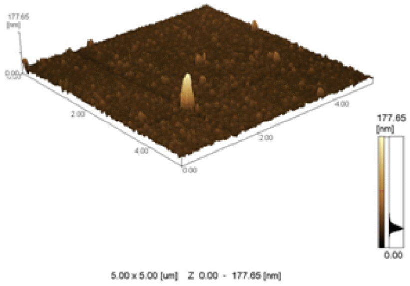

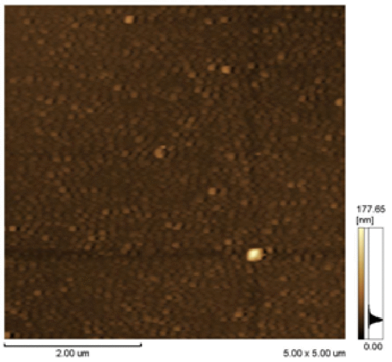

10 Shots

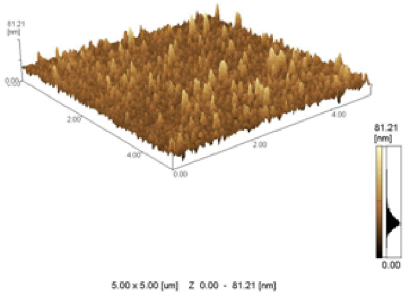

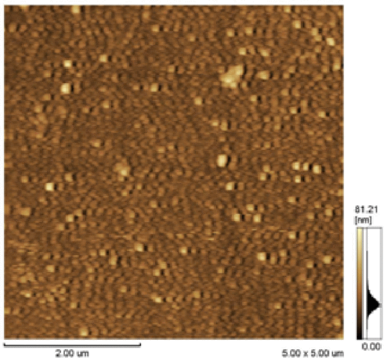

15 Shots

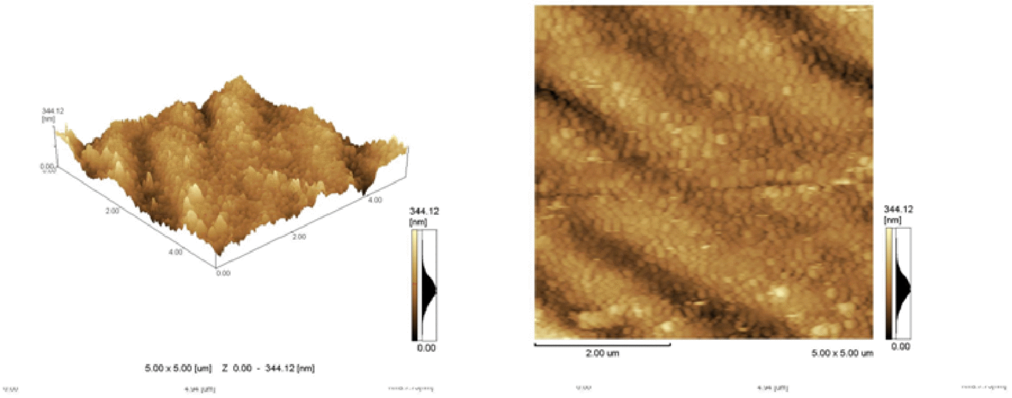

20 Shots

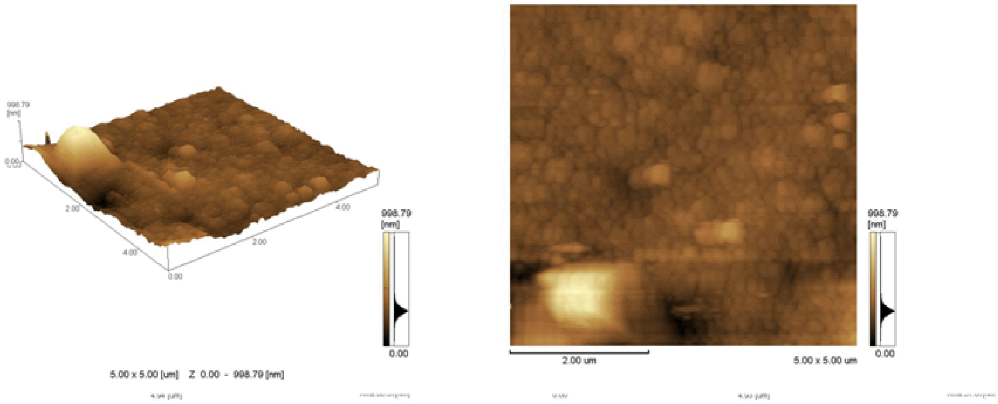

Fig. 6: Topography images of unexposed and exposed samples for 5, 10, 15 and 20 focus shots.

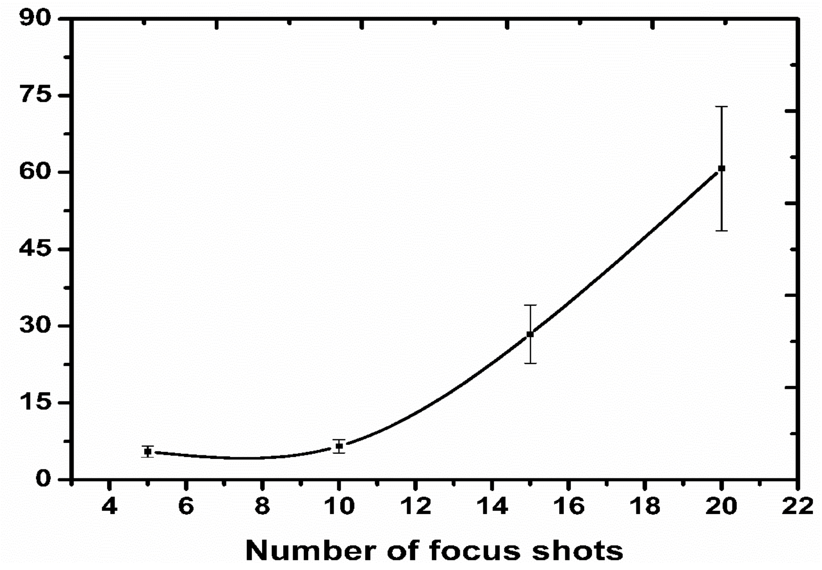

Fig. 7: Roughness of unexposed and exposed samples for 5, 10, 15 and 20 focus shots

To examine and compare the surface roughness of the exposed substrate, in each experiment, the roughness is measured at two random areas over the surface of the deposited film and recorded the average of the root mean square (RMS) values of the measurements. it is because in plasma focus system, the ions are radiated in a fountain-like structure and their flux and energy vary with their angle relative to the anode axis [30]. Hence different areas of the film surface are proved to have different roughness. This diversity is taken into consideration by selecting random areas and computing the average and RMS of their roughness. As the surface topography of exposed substrate shows that the surface roughness increases with the increase in the number of focus shots, which is consistent with SEM micrographs.

3.4. Resistivity Measurement:

The resistivity of WN films synthesized by plasma focus on Si-substrate is determined by four probe technique. The sheet resistivity of a thin film can be determined by the relation,

$$\rho = \frac{\Pi t}{\ln 2}\left(\frac{V}{I}\right)$$

This expression is independent of the probe spacing‘s’. The sheet resistance $R_s = \frac{\rho}{t}$ can be expressed as:

$$R_s = k\left(\frac{V}{I}\right)$$

where the factor ‘k’ is a geometric factor. In the case of a semi-infinite thin sheet, k = 4.53. The factor k will be different for non-ideal samples. The sheet resistance per square of the tungsten nitride thin film prepared for multiple focus shots is shown in figure 8.

It is clear from the graph that the resistivity of all the deposited films is lower as compared to the unexposed substrate which may be due to the formation of tungsten nitride thin film on the substrate surface as the resistivity of tungsten nitride thin films is less as compared to Si-substrate [reference].

Figure 8. shows that the maximum value of sheet resistance for 5 focus shots. The highest value of resistance for 5 shots may be attributed to less tungsten nitride content on the substrate surface. The increase in number of focus shots shows that the resistivity of the substrate surface gradually decreases. It is may be due to the increase in tungsten and nitrogen contents in the deposited WN films with the increase in the number of deposition shots, which is also supported by the XRD, SEM and AFM results.

In fact when grain growth occurs the connectivity between the grains becomes better that enhances the conductivity. The decrease in sheet resistance with increasing number of focus shots may be due to the growth of crystallite size of tungsten nitride films which is due to the increase in crystallized area which probably releases more carriers than the amorphous area [31].

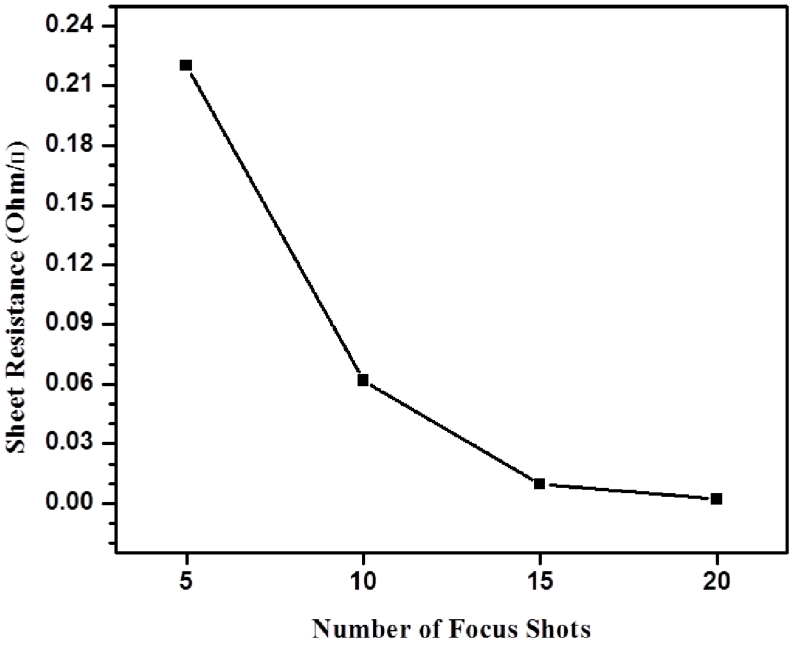

Fig. 8: Variation of sheet resistance as a function of different 5, 10, 15 and 20 focus shots.

Films of smaller grain size have high resistance as compare to larger grains which may be related to the number of dislocations. The grain size and dislocation density are related by the formula

$$\delta = 1/D^2$$

Where ‘D’ is crystallite size and δ is dislocation density. Brown [32] reported that electron mobility is inversely proportional to the density of randomly distributed dislocations. Consequently, the electrical resistance will be proportional to the dislocation density. In polycrystalline materials, the grain boundaries contribute also to the electron scattering and consequently to enhance the electrical resistivity [33].

5. CONCLUSIONS

WN films are deposited on Si-substrate at room temperature by using Mather-type plasma focus system. The energetic charged (electrons/ions) beams emanated from pinched plasma are utilized for the deposition process. The XRD analysis shows the emergence of various phases of tungsten nitride (WN_2, W_5N_4) along with some peaks of silicon nitride (Si_3N_4) onSi-substrate. A small shift in peaks of deposited thin film shows the presence of some residual stresses, which may be caused by the thermal shocks and ion implantation. The crystallite size of both WN_2 (006) and Si_3N_4 (321) phases are ~11 nm and ~16 nm respectively at 10 focus deposition shots. While on increasing number of focus shots, the crystallite size of both phases increases which may be due to the increase in nitrogen and tungsten content in deposited WN films [34]. It shows that the crystallite size of these phases strongly depends on the number of focus shots. The XRD spectra confirm the presences of different phases of WN films on the Si-substrate.

The SEM micrographs show melting effect on the surface of the deposited films, while some pores and cracks are also visible in the micrographs. Surface topography and roughness of the deposited films along with unexposed Si-substrate was carried out by the AFM microscope. The AFM images of the exposed samples show that the increase in surface roughness is increased with the increasing number of focus deposition shots and maximum roughness was observed at 20 focus shots. Tungsten nitride thin films deposited on Si-substrate show the improvement in the conductivity with the increase in number of focus deposition shots. As the number of focus deposition shots increases, the sheet resistance of the deposited film decreases which show the enhancement in the conductivity of the films.

REFERENCES

1. L. E. Toth, Transition metal carbides and nitrides, Academic Press, New York-London (1971).
2. T. Yamamoto, M. Kawate, H. Hasegawa, and T. Suzuki, Surface and Coatings Technology, 193 (2005) 372.
3. T. Polcar, N. M. G. Parreira, and A. Cavaleiro, Wear 262 (2007) 655.
4. T. Polcar, N. M. G. Parreira, and A. Cavaleiro, Wear 265 (2008) 319.
5. M. H. Tsai, S. C. Sun, H. T. Chiu, and S. H. Chuang, Applied Physics Letters, 68 (1996) 1412.
6. K. M. Chang, T. H. Yeh, and I. C. Deng, Journal of Applied Physics, 81 (1997) 3670.
7. S. Bystrova, A. A. I. Aarnink, J. Holleman, and R. A. M. Wolters, Journal of the Electrochemical Society, 152 (2005) G522.
8. S. Bong, Y. J. Lee, J. S. Hwang, and C. O. Park, Thin Solid Films, 348 (1999) 299.
9. G. Soto, W. de la Cruz, F. F. Castillón, J. A. Díaz, R. Machorro, and M. H. Farías, Applied Surface Science, 214 (2003) 58.
10. M. T. Hosseinnejad, M. Ghoranneviss, G. R. Etaati, M. Shirazi, and Z. Ghorannevis, Applied Surface Science, 257 (2011) 7653.

11. T. Migita, R. Kamei, T. Tanaka, and K. Kawabata, Applied Surface Science, 169 (2001) 362.
12. T. Hussain, R. Ahmad, I. Khan, J. Siddiqui, N. Khalid, A. S. Bhatti, and S. Naseem, Nuclear Instruments and Methods in Physics Research Section B: Beam Interactions with Materials and Atoms, 267 (2009) 768.
13. A. Hussnain, R. S. Rawat, R. Ahmad, T. Hussain, Z. A. Umar, U. Ikhlaq, Z. Chen, and L. Shen, Radiation Effects and Defects in Solids, 170 (2015) 73.
14. R. S. Rawat, Nanoscience and Nanotechnology Letters, 4 (2013) 251.
15. R. Ahmad, M. Hassan, G. Murtaza, A. Waheed, and M. Zakaullah, Journal of Fusion Energy, 21 (2002) 217.
16. I. A. Khan, S. Jabbar, T. Hussain, M. Hassan, R. Ahmad, M. Zakaullah, and R. S. Rawat, Nuclear Instruments and Methods in Physics Research Section B: Beam Interactions with Materials and Atoms, 268 (2010) 2228.
17. R. Rawat, W. Chew, P. Lee, T. White, and S. Lee, Surface and Coatings Technology, 173 (2003) 276.
18. M. Hassan, R. Ahmad, A. Qayyum, G. Murtaza, A. Waheed, and M. Zakaullah, Vacuum, 81 (2006) 291.
19. R. S. Rawat, P. Lee, S. Lee, P. Arun, and A. G. Videshwar, AIP Conference Proceedings, 669 (2003) 343.
20. R. S. Rawat, W. M. Chew, P. Lee, T. White, and S. Lee, Surface and Coatings Technology, 173 (2003) 276.
21. J. Siddiqui, T. Hussain, R. Ahmad, W. Ali, A. Hussnain, and R. Ayub, Journal of Fusion Energy, 34 (2015) 1193.
22. T. Hussain, R. Ahmad, N. Khalid, Z. Umar, and A. Hussnain, Nuclear Instruments and Methods in Physics Research Section B: Beam Interactions with Materials and Atoms, 269 (2011) 1951.
23. A. HUSSNAIN, R. Ahmad, T. Hussain, Z. A. Umar, N. Khalid, and A. Saeed, Journal of Natural Sciences and Mathematics, 51 (2011) 13.
24. T. Hussain, R. Ahmad, N. Khalid, Z. A. Umar, and A. Hussnain, Nuclear Instruments and Methods in Physics Research Section B: Beam Interactions with Materials and Atoms, 269 (2011) 1951.
25. R. Rawat, P. Lee, T. White, L. Ying, and S. Lee, Surface and Coatings Technology, 138 (2001) 159.
26. M. Sadowski, H. Schmidt, and H. Herold, Physics Letters A, 83 (1981) 435.
27. B. D. Cullity and S. R. Stock, Elements of x-ray diffraction, Prentice Hall, (2001).
28. G. Gerdin, W. Stygar, and F. Venneri, Journal of Applied Physics, 52 (1981) 3269.

29. R. S. Rawat, W. M. Chew, P. Lee, T. White, and S. Lee, Surface & Coatings Technology, 173 (2003) 276.
30. L. Bertalot, H. Herold, U. Jäger, A. Mozer, T. Oppenländer, M. Sadowski, and H. Schmidt, Physics Letters A, 79 (1980) 389.
31. S. K. Bahl and K. L. Chopra, Journal of Applied Physics, 41 (1970) 2196.
32. R. A. Brown, Journal of Physics F: Metal Physics, 7 (1977) 1283.
33. D. Rafaja, H. Köstenbauer, U. Mühle, C. Löffler, G. Schreiber, M. Kathrein, and J. Winkler, Thin Solid Films, 528 (2013) 42.
34. A. Hussnain, R. Rawat, T. Seng, R. Ahmad, T. Hussain, P. Lee, C. Zhong, S. Lu, and Z. Zheng, Journal of Fusion Energy, 34 (2015) 435.

PK ISSN 0022- 2941; CODEN JNSMAC
Vol. 55, (2015) PP 35-45

SYNTHESIS, STRUCTURAL, AND MAGNETIC PROPERTIES OF Fe DOPED SnO_2 NANOMATERIALS

G. FARID[*1,2], M. SUFYAN[2], A. WAHAB[2], M. UMAIR[1], J. I. SAGGU[2]

[1]Centre for Advanced Studies in Physics, Government College University Lahore, Pakistan.

[2]FBAS, International Islamic University Islamabad.

*E-mail address: ghulam.mscphys173@iiu.edu.pk

(Received: 05-04-2016)

ABSTRACT: Fe doped SnO_2 nanoparticles have been prepared using simple, cheap and quick wet chemical route at ambient temperature. The morphological investigations using scanning electron microscope have shown that the prepared samples are nanoparticles in the range of 89-114 nm. The crystal structure and phase purity of Fe nanoparticles have been examined using X-ray diffraction. The prepared nanoparticles exhibit single phase SnO_2 Rutile and no extra peak is observed. The crystallite size is calculated by the XRD which is in nm range and in good agreement with the SEM results. Substitution of Fe into the SnO_2 is confirmed by the peak shifting in XRD patterns. The peaks observed in FTIR spectra is in good agreement with the presence of Sn-O terminal bond of SnO_2 and C=O in carboxylic acid or carbonyl impurities. The prepared SnO_2 nanoparticles exhibits diamagnetism, while doping of Fe into it leads towards the room temperature ferromagnetism. M-H loop for undopedSnO_2 shows typical diamagnetic behavior. The diamagnetism is due to the presence of paired electrons in its “d” orbital.

Keywords: Nanomaterials, Doping, Rutile, Diamagnetism,

1. INTRODUCTION

Since the advent of nanotechnology, Diluted magnetic semiconductors have gain more attention, a lot of researchers are working in order to enhance and optimize their magnetic, optical, electrical and chemical properties. Some researcher, studied nanoparticle prepared by chemical methods, found ferromagnetic behavior [1,2,3,4], while other reported paramagnetic and antiferromagnetic [5,6]. SnO_2 nanoparticles have been prepared by various method like sol-gel routes, inorganic [7], organometallic [8], co-precipitation [9], chemical precipitation [10], hydrothermal methods [11], microwaves assisted synthesis [12] and polyol method [13-15]. In particular, the sol gel is one of the most attractive one, due to its low cost, the ability to control the grain size and its short preparation time. To modify the properties SnO_2doping is among the best factor. Tin dioxide was doped successfully with different transition metal, such as Fe[16], Ni[17,18], Co[19,20], Mn[21,22], Cr[23]and V[24]

Especially DMS's whose curie temperature is above room temperature are of great interest because of their application in the field of sensors, detectors, memory devices, possible photo voltaic applications, light emitting devices ,catalysis and spintronic devices. SnO_2 is widely used DMSs due to its application in the field of memory devices. For the next generation spintronic devices Fe doped SnO_2semiconductors are potential materials. Some authors have done studies on room temperature ferromagnetism in transition metal-doped SnO_2semiconductor. In this field, certain issue is still under debate, for example, in these materials magnetic moment values, a large range of Curie temperature values and magnetic order have been reported depending on the transition metal concentration and the preparation technique.

A wide band gap SnO_2 (3.6 eV–3.8 eV) has attracted considerable attention whenever doped with transition metal (TM) ions (Fe, Cu, etc.) because of their remarkable electronic, optical and magnetic properties resulting from large sp–d exchange interactions between the magnetic ions and the band electrons [25,26]. Iron doping in SnO_2 was expected to have significant effect of its magnetic properties due to availability of unpaired electrons [27]. SnO_2 is basically a diamagnetic substance by incorporating iron its magnetic properties can be enhanced due to unpaired electrons of iron and it became paramagnetic substance. By incorporating iron in SnO_2 structure, spin due to iron atom show magnetization and overall property of the material be change.

The aim of this research work was to investigate the magnetic property of Fe doped SnO_2. By using theses characterization techniques XRD, SEM, FTIR, VSM we studied structural, morphological, chemical and magnetic properties respectively. As doping effect change the properties of our material from diamagnetic to paramagnetic and it is confirmed by VSM.

2. EXPERIMENTAL PROCEDURE

The sol gel method is, a wet chemical way for the fabrication of colloidal dispersions of inorganic and organic hybrid materials particularly oxide and oxide based hybrid .From such colloidal dispersion, fibers, powder and thin films can easily be prepared. The fabrication are the same, Through the synthesis of different kind of final structures needs particular consideration, some basic and general approaches. A number of factors are associated with the characteristics and properties of a specific sol gel inorganic complex, such as PH values, time of reaction, reagent concentration, concentration, drying, catalyst nature and temperature. To very the structure and properties of the sol gel derived inorganic network over wide ranges by controlling these factors.

The tin dioxide nanoparticles were prepared by the sol–gel method. In a typical procedure, 6 g hydrated tin chloride ($SnCl_2$ _$2H_2O$) was dissolved impure ethanol (C_2H_5OH). The solution was stirred with a magnetic stirrer for 30 min in a flask. About 5 ml of acetyl acetone (AcAc) was added drop wise to control the particle size of SnO_2. Now 6g of Polyethylene glycol PEG was applied as a chemical modifier reagent. Then we add 5 ml of ammonia drop wise for hydrolysis of SnO_2. Now we stirrer the solution for 1 h after this the solution was continuously refluxed at 80°C to form the SnO_2 sol solution. Then the solution was twice centrifuge for separate the precipitate and after this the solution was placed in oven at 80°c for 16 hrs. Now we grind the solid sample and again placed in oven at 300°c for 3 h for annealing [28].

3. RESULTS AND DISCUSSION

3.1. Structural Analysis of Fe-Doped SnO_2 Nanoparticles:

To check the crystal structure, composition and phase analysis of undopedSnO_2 and Fe doped SnO_2 nanostructures in powder form, synthesize by sol gel method were characterized by XRD using X-ray of wavelength (λ =1.5405 Å) radiation. The XRD patterns of undopedSnO_2 and 1%, 3%, 5%, Fe doped SnO_2 nanostructures annealed at 300C shows that all diffraction peaks can be readily indexed to SnO_2 nanoparticles. No extra peaks were observed, which indicates the purity of the samples. The occurrence of broad peaks in these figures confirms the nano crystalline nature of these samples. The value of both lattice constants “a” and “c” were found to decrease from 4.724 to 4.694 Å and 3.232 to 3.205 Å, respectively, with the rise of the Cu contents in the series of the samples The crystallite size has been estimated from the X-ray peak broadening, taking into consideration the most intense diffraction peak (110) for all the samples. The evaluated values of the crystallite size were found to vary from 57.2 to 48.7.

By using Bragg's law d spacing is determined [29].

$2dSin\theta = n\lambda$.......................... 4.1

Taking n=1 and λ as wavelength of X rays 1.5405 Å

$d=\lambda/2\sin\theta$.............................. 4.2

By Using Scherrer formula the crystallite size (**d**) is calculated;

d= $k\lambda/\beta\cos\theta$........................... 4.3

Where , λ is the wavelength of the X rays which is 1.54 **Å** ,K is a shape constant whose value is 0.9, β is full wave half maximum (FWHM). The values of d spacing, peak angle, crystallite size and corresponding planes for each sample are given in the table below;

Table 4.1 Values of Lattice Parameter, crystallite size of Pure and Fe doped SnO2

Sample	a=b(Å)	c(Å)	a/c ratio	Crystallite size (nm)	Cell Volume (Å)^3
Undoped SnO_2	4.724	3.232	1.46	57.2±0.122%	62.46
$Fe_{0\cdot03}Sn_{0.97}O_2$	4.612	3.220	1.43	57.1±0.180%	59.36
$Fe_{0\cdot05}Sn_{0.95}O_2$	4.604	3.205	1.42	48.7±0.1651%	58.83

The combined XRD pattern shows that Fe is successfully doped in SnO_2 as all the main peaks of the pattern satisfy the standard card of the SnO_2. The intensity is increases by increasing the concentration of Fe. We can also see the little shifting of the peaks toward higher angle as concentration of Fe is increased. The XRD spectra illustrate that the Rutile phase formed. A contraction in lattice volume was observed in Fe doped SnO_2 prepared by Liuetal. [30] And was explained by the incorporation of smaller Fe^{3+} (0.49 Å) ions replacing larger Sn^{4+} (0.55 Å) ions. Volume of the unit cell is also decrease as the Fe doping concentration is increase [31]. The Fe-doping not only reduce the crystalline size but also change the size of the nanoparticles. Decrease in crystalline size of Fe-doped SnO_2 nanoparticles in contrast with the pure SnO_2 due to the decrease in the intensity of SnO_2 peaks.

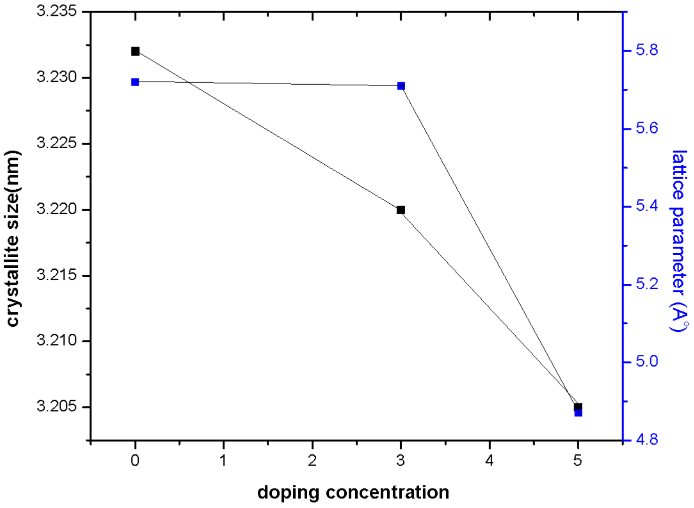

Fig.1: Plot of Crystalline size, Lattice Parameter against concentration

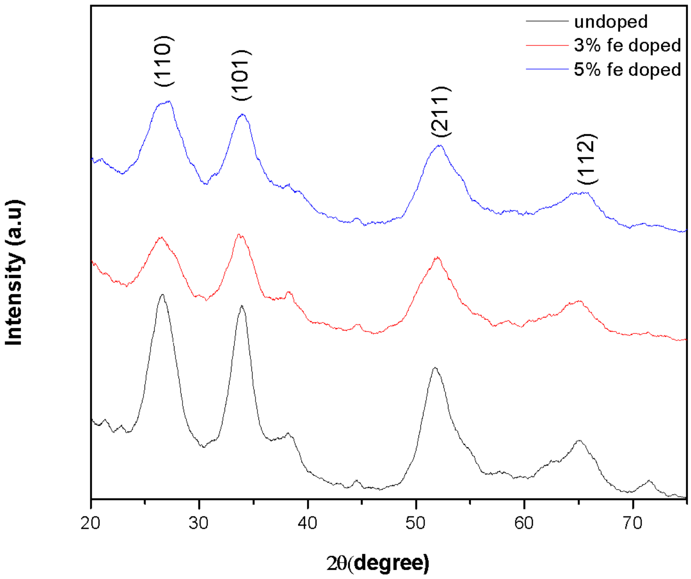

Fig.2: Combined XRD pattern of pure, 3%and 5% Fe doped SnO2 samples

3.2. Morphological Analysis:

The surface morphology of undoped and Fe doped SnO_2 samples have been observed using SEM. The SEM micrographs ofSnO_2 with varying Fe doping levels are shown in figure 4.3.

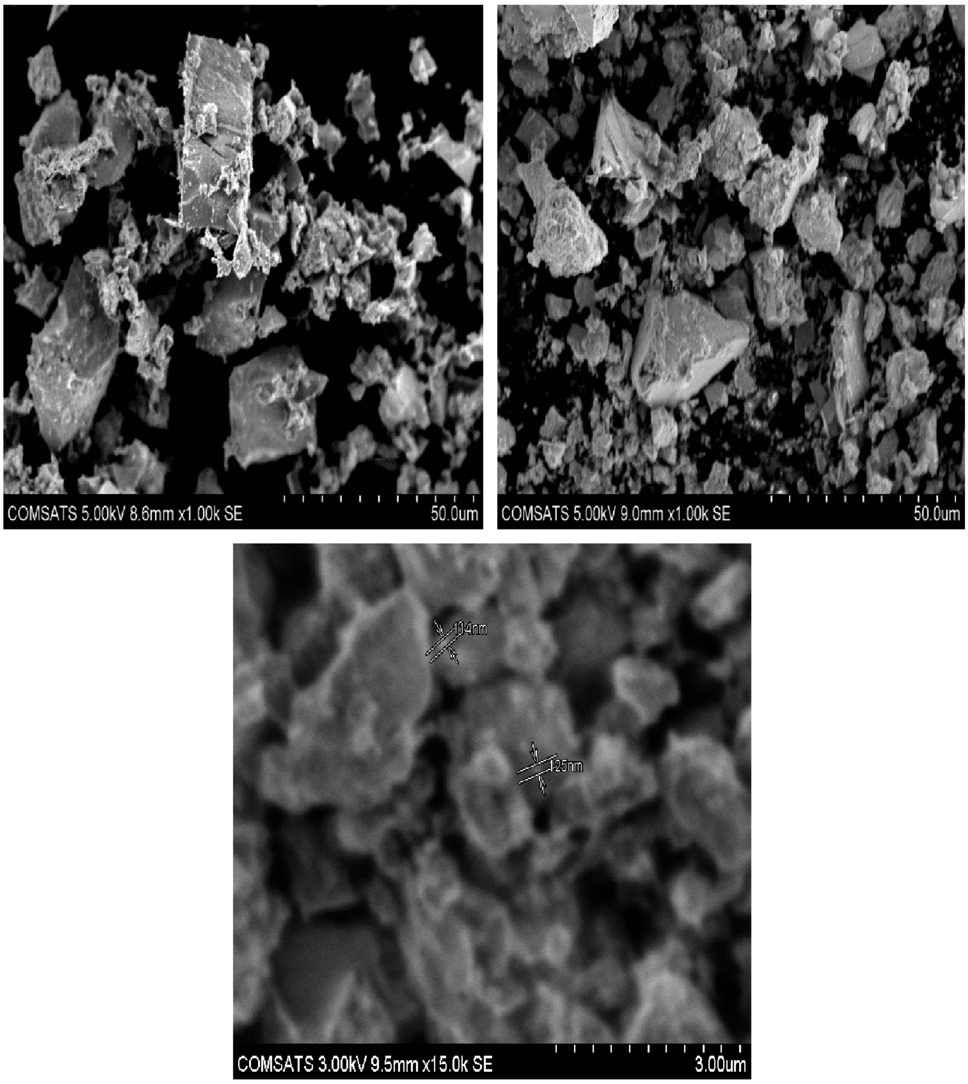

Fig.3: SEM images **(a)** undopedSnO2 **(b)** 3% Fe doped SnO2 (**c)** 5% Fe doped SnO2.

Figure 4.3 (a) shows the morphology of un-doped SnO_2 sample, it is clear from the figure the clusters form nanoparticles are formed and this cluster form is due to the annealing temperature (at 300°C). In addition the morphology of SnO_2 nanocrystals strongly depends on the annealing temperature especially in $T \geq 500°C$ the size of nanocrystals with tetragonal structure is increased [30].The grain size of undoped SnO_2 has been found to be 30 nm. In Figure 4.3 (b) with Fe doping of 3% the spherical grain morphology of particles is observed. The grain size of$Fe_{0.03}Sn_{0.97}O_2$is approximately 74.9nm.Further in Fig 4.3(c) with Fe doping of 5% the grain size of particles is increases and the noted size of $Fe_{0.05}Sn_{0.95}O_2$ is 114nm. The average grain size is 89.6 nm In fig 4.3(b) some small particles can also be seen on the surface of large particles. Same is the case in Figure 4.2 (c) where clusters further grow in size and make larger particles. However some aggregation of nanoparticles has also observed in all SEM micrographs. This aggregation in synthesized nanoparticles is expected due to theOH- ions in sample. [32]

Table.4.2: Grain size of particles with different doping concentration of Fe in SnO2

Sr no.	Samples (Doping level)	Average grain size (nm)
1	Undoped Sno_2	75.4nm
2	$Fe_{0.03}Sn_{0.97}O_2$	79.4nm
3	$Fe_{0.05}Sn_{0.95}O_2$	114nm

3.3. FTIR Analysis:

FTIR is a powerful technique to find out the information about the chemical bonding in a material, identify the elemental constituents of a material sample and supplements the information obtained from XRD and SEM. FTIR spectra were recorded in solid phase using KBr pellet technique in the wavenumber region 4000– 400cm^{-1} for all Fe doped SnO_2 samples are shown in Fig. This spectral region is very important because of several stretch modes involving hydroxyl bond, carbon to oxygen and metal oxide bonds are obtained clearly in this range.[33] The peak at 497 cm^{-1} is assigned to the Sn-O terminal bond of SnO_2.[34] The peak at 1220 cm^{-1} is assigned to the bending vibrations of –CH2 and –CH3, which shows that a few organic groups are absorbed on the surfaces of SnO_2 nanoparticles. [35] The peak at 1364 cm^{-1}is assigned to the bending vibration of NO_3^- ions. [34]. The characteristic peak at 1735 cm^{-1}is assigned to the stretching band of C=O in carboxylic acid or car-bonyl moieties.[36]

The peak at 2365 cm $^{-1}$ is assigned to the existence of CO_2 molecule in air.[37] In the graph the peak is shifted towards the lower wave number that increase the oxygen vacancies lead the metal oxygen vibration to lower values. This is because the bond gets weakened due to the unavailability of oxygen.[38] Hence we conclude that our doping is successfully done. The “Fe” successfully replace the “Sn” atom. And no extra peak is observed.

Table 2: IR frequencies and band assignment for the pure SnO_2 and Fe doped SnO_2 samples

Wavenumber (cm^{-1})	**Band Assignment**
497 cm^{-1}	Sn-O
1220 cm^{-1}	–CH2 and –CH3
1364 cm^{-1}	NO_3^-
1735 cm^{-1}	C=O
2365 cm^{-1}	CO_2

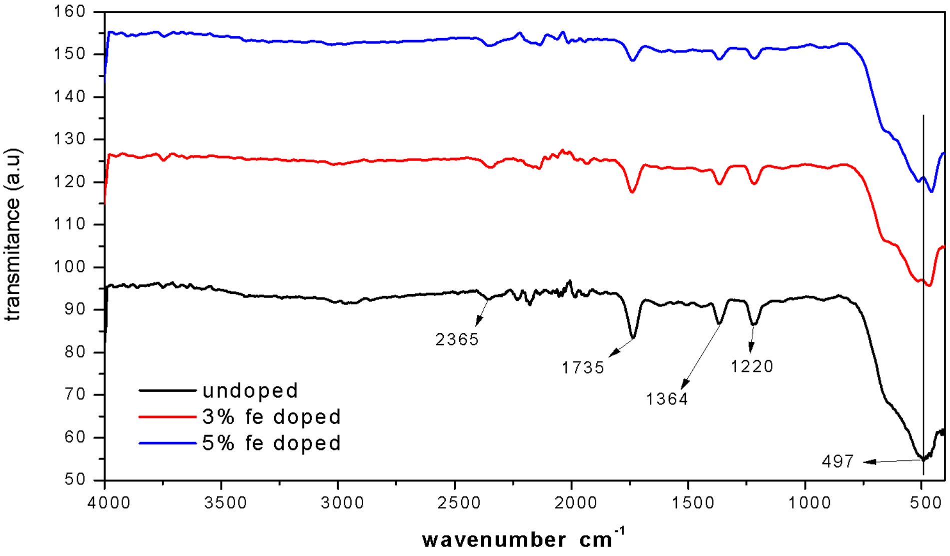

Fig.4: Combined FTIR pattern of pure SnO2 and Fe doped SnO2 samples

3.4. Magnetic Characterization:

The dependence of magnetization on magnetic field at room temperature was studied for pure SnO_2 and Fe doped SnO_2 nanoparticles. M-H loop for undopedSnO_2 shows typical diamagnetic behavior. The diamagnetism is due to the presence of paired electrons in its d orbital. In addition, Fe-doped SnO_2 samples for composition (3%) measured at 300k shows that the variation of magnetization with magnetic field is linear indicating Weak Ferromagnetic behavior. The figure 4.5 is showing the MH-loop for (3%). In this weak ferromagnetic state all moments are moderately aligned. This Weak ferromagnetism behavior is due to the less amount of Iron concentration.

The overall ferromagnetic behavior is systematically increasing with the increase of dopant concentration which is shown in figure 4.The weak Ferromagnetism observed may have resulted due to the following reasons .The inhomogeneous distribution of Fe atoms in the host lattice may cause shorter distance between a pair of transition metal ions giving rise to ferromagnetism [39].

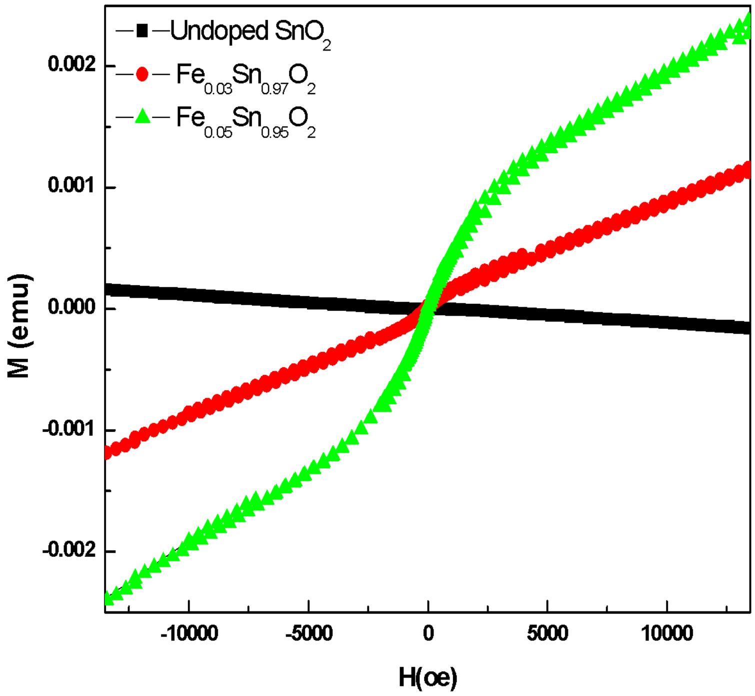

Fig.5: The M–H curves of Fe-doped SnO2 nanoparticles with Fe concentration: (0%, 3%, and 5%,)

The figure 4.5 is also showing the MH-loop for (5%). In this Figure Strong ferromagnetic curve is observed. In these strong ferromagnetic states all moments are totally aligned. This Strong ferromagnetism behavior is due to the large amount of Iron concentration.

4. CONCLUSIONS

The synthesis of undoped SnO_2 and Fe doped SnO_2 nanostructures have been carried out via a simple, efficient and versatile sol-gel method. The structural and morphological study has been performed through XRD and SEM. The magnetic properties have been analyzed using VSM. It has been concluded that:

- Successful synthesis of SnO_2 Nanostructures by simple Sol-gel method.

- Successful doping of Fe into SnO_2 host matrix.
- From FTIR result bonding of tin dioxide is confirmed.
- Furthermore, it is observed from FTIR results that number of oxygen vacancies increases with Fe doping.
- The magnetic properties shows the ferromagnetic behavior of Fe doped SnO_2

REFERENCES

1. C. B. Fitzgerald, M. Venkatesan, A. P. Douvalis, S. Huber, J. M. D. Coey and T. Bakas, J. Appl. Phys., 95 (11) (2004) 7390.
2. A. Punnoose, J. Hays, A. Thurber, M.H. Engelhard, R.K. Kukkadapou, C. Wang, V. Shutthanandan and S. Thevuthasan, Phys. Rev. B, 72 (2005) 054402.
3. K. Galatsis, L. Cukrov, W. Wlodarski, P. McCormick, K. Kalantar-zadeh, E. Comini and G. Sberveglieri, Sensors and Actuators B, 93 (1-3) (2003) 562.
4. A. Punnoose, J. Hays, V. Gopal and V. Shutthanandan, Appl. Phys. Lett., 85 (9) (2004) 1559.
5. C. M. Liu, X. T. Zu, W. L. Zhou, J. Phys. Condens. Matter, 18 (2006) 6001.
6. N. Dave, B. G. Paulter, S. S. Farvid and P. V. Radovanovic, Nanotechnology, 21 (2010) 134023.
7. G. Zhang and M. Liu, J. Mater. Sci., 34 (1999) 3213.
8. L. Renard, O. Babot, H. Saadaoui, H. Füess, J. Brötz, A. Gurlo, E. Arvaux, A. Klein and T. Toupance, Nanoscale, 4 (2012) 6806.
9. H. Yang, Xiaolan Song, X. Zhang, W. Ao and G. Qiu, Mater. Lett., 57 (2003) 3124.
10. K. C. Song and Y. Kang, Mater. Lett., 42 (2000) 283–289.
11. H. C. Chiu and C. S. Yeh, J. Phys. Chem. C, 111 (2007) 7256.
12. J. J. Zhu, J. M. Zhu, X. H. Liao, J. L. Fang, M. G. Zhou and H. Y. Chen, Mater. Lett., 53 (2002) 12.
13. X. Jiang, Y. Wang, T. Herricks and Y. Xia, J. Mater. Chem., 14 (2004) 695.
14. R. Sasikala, A. Shirole, V. Sudarsan, T. Sakuntala, C. Sudakar, R. Naik and S. R. Bharadwaj, Int. J. Hydrogen Energy, 34 (2009) 3621.
15. J. Ren, J. Yang, A. Abouimrane, D. Wan and, K. Amine, J. Power Sources, 196 (2011) 8701.
16. J. Sakuma and K. Nomura, Thin Solid Films, 515 (2007) 8653.
17. C. M. Liu, L. M. Fang, X. T. Zu and W. L. Zhou, Phys. Scr., 80 (2009) 065703.

18. S. Zhuang, X. Xun, Y. Pang, H. Li, B. Yu and J. Hu, J. Magn. Magn. Mater., 327 (2013) 24.
19. A. M. Abdel Hakeem, J. Magn. Magn. Mater., 324 (2012) 95.
20. P. Chetri and A. Choudhury, J. Alloys Comp., 627 (2015) 261.
21. L. Zhang and S. Ge, Scr. Mater. 63 (2010) 953.
22. C. T. Wang and M. T. Chen, Sens. Actuators: B. Chem., 150 (2010) 360.
23. B. Liu, X. Wang, G. Cai, L. Wen, Y. Song, X. Zhao, J. Hazard. Mater., 169 (2009) 1112.
24. D. Toloman, A. Popa, O. Raita, M. Stan, R. Suciu, M. O. Miclaus and A. R. Biris, Opt. Mater., 37 (2014) 223.
25. J. Kaur, J. Shah, R. K. Kotnala and K. C. Verma, Ceram. Int., 38 (2012), 5563.
26. S. Nilavazhagan and S. Muthukumaran, Superlattices and Microstructures, 83 (2015) 507.
27. J. Sakuma and K. Nomura, Thin Solid Films, 515 (2007) 8653.
28. T. Dietl, H.Ohno, M. Matsukura, J. Cibert, and D. Ferrand, Science, 287 (2000) 1019.
29. Y. J. Kwon, K. H. Kim and C. S. Lim, Journal of Ceram Proc. Res., 3 (2002) 146.
30. J. F. Liu, M. F. Lu, P. Chai, L. Fu, Z. L. Wang, X. Q. Cao and J. Meng, J. Magn. Magn. Mater., 317, 1 (2007) 1.
31. V. Bilovol, C. Herme, S. Jacobo and A. F. Cabrera, Materials Chemistry and Physics, 135 (2012) 334.
32. M. M. Bagheri-Mohagheghi, N. Shahtahmasebi, M. R. Alinejad, A. Youssefi, M. Shokooh-Saremi, Physica B: Condensed Matter, 403 (13-16) (2008) 2431.
33. S. Das, S. Kar and S. Choudhary, J. Appl. Phys., 99 (2006) 114303.
34. M. M. Hassan, W. Khan, A. Azam and A. H. Naqvi, Journal of Luminescence, 145 (2014) 160.
35. R. N. Mariammal, N. Rajamanickam and K. Ramachandran, Journal of Nano- and Electronic Materials, 3 (1) (2011) 92.
36. S. Gnanam and V. Rajendran, J. Sol-Gel Sci. Technol., 56 (2010) 128.
37. X. Li, X. Xu, X. Yin, C. Li and J. Zhang, Particuology, 9 (5) (2011) 471.
38. M. P. Deosarkar, S. M. Pawar, S. H. Sonawane, B. A. Bhanvase, Chem. Eng. Processing: Process Intensification, 70 (2013) 48.
39. P. Chetri, B. Saikia, A. Choudhury, J. Appl. Phys., 113 (2013) 233514.

PK ISSN 0022- 2941; CODEN JNSMAC
Vol. 55, (2015) PP 47-60

ATHEROSCLEROTIC STUDY OF TWO DIMENSIONAL BLOOD FLOW OF AN OLDROYD-B FLUID THROUGH AN ARTERY

A. A. MIRZA*[1], A. M.SIDDIQUI[2], T. HAROON[1]

[1]Department of Mathematics, COMSATS Institute of Information Technology, Park Road, ChakShahzad, Islamabad, Pakistan.
[2]Department of Mathematics, Pennsylvania State University, York Campus, 1031Edgecomb Avenue, York, PA 17403, USA.
*E-mail address:azharali_mirza1@yahoo.com

(Received: 05-04-2016)

ABSTRACT: The analysis is concerned with the hemodynamic behavior of blood flow in the artery having arterial constriction. The radius of the artery is R_o and blood is assumed to be Oldroyd-B fluid which is independent of time. The governing Navier-Stokes equations are reduced to stream function formulation by transformation. The regular perturbation technique is applied to find the analytical solution of highly non-linear equations by considering δ as a small parameter. The analytical solutions as well as numerical solutions through graphs for stream lines, wall shear stress, separation and reattachment points and pressure gradient are presented. At the end comparison of our result with the existing results and deduction of results are presented which ensures good agreement.

Keywords: Oldroyd-B fluid, wall shear stress, pressure distribution.

1. INTRODUCTION

It is well known that the deposit of cholesterol and proliferation of connective tissue may be responsible for the abnormal growths in the lumen of the artery. The actual cause is not known exactly but its effect on cardiovascular system can easily be understood by studying the blood flow in its vicinity. Many authors studied the behavior of blood in the constricted artery and they considered the blood as a Newtonian and non-Newtonian fluid, the most earliest and basic paper about blood flow is Young [1] in which he suggested that the boundary irregularities can be an important factor in the development and progression of arterial disease. Forrester and Young [2] presented the analytical solution of Newtonian fluid for axisymmetric, steady, incompressible flow and considered the mild constriction for the flow of blood both theoretically and experimentally in the converging and diverging tube. Lee and

Fung [3] solved the problem of blood flow through constricted artery numerically. Morgan and Young [4] presented the approximate analytical solution of axisymmetric, steady which is applicable to both mild and severe constriction by using an integral method; basically they presented the extension of [2]. K. Haldar [5] investigated the blood flow through an axisymmetric constricted artery and considered the constriction of cosine shape. Chow *et al.*[6] presented solution for symmetric channel with sinusoidal wall variation. One of the practical application is blood flowing through membrane oxygenator with irregular wall surface. Many authors studied the behavior of blood as a non-Newtonian fluid due to its suspension of cells at low shear rate. Shukla*et al.*[7] presented the analysis by considering blood as non-Newtonian fluid and studied the effect of constriction on the resistance to flow and wall shear stress in an artery. Mishra and Shit [8] considered the Herschel – Bulkley equation to represent the non-Newtonian character of blood. Haldar [9] discussed the effect of shape for constriction on the resistance of blood flow through an artery with mild local narrowing. Cheng and Michel [10] discussed the blood as steady and pulsatile physiological flows.

In this analysis, blood is considered as steady incompressible Oldroyd-B fluid and analytical solutions are presented by using the regular perturbation technique. Numerically through graphs the effect of stream lines, wall shear stress, points of separation and reattachment, velocity distribution and pressure gradient are presented.

2. PROBLEM FORMULATION

Assume that the blood is flowing through an axisymmetric artery of infinite length and having the constriction of length $l_o/2$. The coordinate system is chosen in such a way that the arterial system lies in the r z - plane having z - axis coincide with the center line in the direction of flow and r - axis is perpendicular to z - axis.

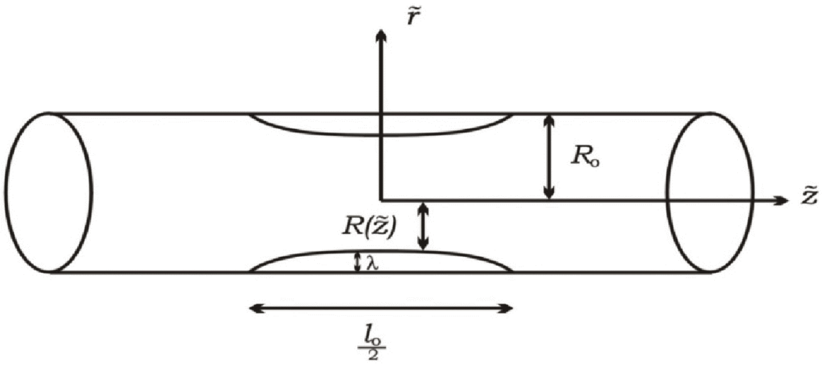

Fig.1. Geometry of the problem.

The boundary of the constricted region is considered of the form [5].where $R(\tilde{z})$ is variable gap due to stenosis,

Introducing the dimensionless quantities as follows

$$z = \frac{\tilde{z}}{l_o}, \quad r = \frac{\tilde{r}}{R_o}, \quad u = \frac{\tilde{u}}{u_o}, \quad w = \frac{\tilde{w}}{u_o}, \quad p = \frac{R_o^2}{\mu u_o l_o}\tilde{p}, \quad S = \frac{R_o}{\mu u_o}\tilde{S}, \qquad (1)$$

Where u_o is the average velocity and $2R_o$ the width of an unobstructed artery. Dimensionless form of the boundary profile is

$$\begin{aligned} f(z) &= 1 - \frac{\varepsilon}{2}\left(1 + \cos(4\pi z)\right) \qquad && -\frac{1}{4} < z < \frac{1}{4}, \\ &= 1 && \text{otherwise}, \end{aligned} \qquad (2)$$

Where ε is the maximum height of constriction. Introducing the stream functions for the velocity components as follows

$$u = \frac{\delta}{r}\frac{\partial \psi}{\partial z}, \quad w = -\frac{1}{r}\frac{\partial \psi}{\partial r}, \qquad (3)$$

which satisfy the continuity equation identically and component form of momentum and constitutive equation in terms of stream function becomes

$$\frac{\partial q}{\partial r} - \frac{\mathrm{Re}\,\delta}{r^2}\left(\frac{\partial \psi}{\partial r}\right)\nabla^2\psi = \frac{\delta}{r}\frac{\partial (rS_{rr})}{\partial r} + \delta^2\frac{\partial S_{rz}}{\partial z} - \delta\frac{S_{\theta\theta}}{r}, \qquad (4)$$

$$\frac{\partial q}{\partial z} - \frac{\mathrm{Re}\,\delta}{r^2}\left(\frac{\partial \psi}{\partial z}\right)\nabla^2\psi = \frac{1}{r}\frac{\partial (rS_{rz})}{\partial r} + \delta\frac{\partial S_{zz}}{\partial z}, \qquad (5)$$

$$\begin{aligned} &S_{rr} + \alpha\left\{\frac{\delta}{r}\frac{\partial(\psi, S_{rr})}{\partial(z,r)} - 2S_{rr}\delta\frac{\partial}{\partial r}\left(\frac{1}{r}\frac{\partial \psi}{\partial z}\right) - 2\frac{\delta^2}{r}S_{rz}\frac{\partial^2 \psi}{\partial z^2}\right\} = 2\delta\frac{\partial}{\partial r}\left(\frac{1}{r}\frac{\partial \psi}{\partial z}\right) \\ &+\beta\left\{\frac{2\delta^2}{r}\frac{\partial\left(\psi, \frac{\partial}{\partial r}\left(\frac{1}{r}\frac{\partial \psi}{\partial z}\right)\right)}{\partial(z,r)} - 4\delta^2\left(\frac{\partial}{\partial r}\left(\frac{1}{r}\frac{\partial \psi}{\partial z}\right)\right)^2 - \frac{2\delta^2}{r}\frac{\partial^2 \psi}{\partial z^2}\left(\frac{\delta^2}{r}\frac{\partial^2 \psi}{\partial z^2} - \frac{\partial}{\partial r}\left(\frac{1}{r}\frac{\partial \psi}{\partial z}\right)\right)\right\}, \end{aligned} \qquad (6)$$

$$S_{r\theta} + \alpha\left\{\frac{\delta}{r}\frac{\partial(\psi, S_{r\theta})}{\partial(z,r)} - S_{r\theta}\frac{\delta}{r}\frac{\partial^2 \psi}{\partial r \partial z} - \frac{\delta^2}{r}S_{z\theta}\frac{\partial^2 \psi}{\partial z^2}\right\} = 0, \qquad (7)$$

$$\begin{aligned}&S_{rz}+\alpha\left\{\frac{\delta}{r}\frac{\partial(\psi,S_{rz})}{\partial(z,r)}+S_{rr}\delta\frac{\partial}{\partial r}\left(\frac{1}{r}\frac{\partial\psi}{\partial r}\right)-\frac{\delta^2}{r}S_{zz}\frac{\partial^2\psi}{\partial z^2}+\frac{\delta}{r^2}S_{rz}\frac{\partial\psi}{\partial z}\right\}=\frac{\delta^2}{r}\frac{\partial^2\psi}{\partial z^2}-\frac{\partial}{\partial r}\left(\frac{1}{r}\frac{\partial\psi}{\partial r}\right)\\&+\beta\left\{\left\{\frac{\delta}{r}\left(\frac{\partial\psi}{\partial z}\frac{\partial}{\partial r}-\frac{\partial\psi}{\partial r}\frac{\partial}{\partial z}\right)+\frac{\delta}{r^2}\frac{\partial\psi}{\partial z}\right\}\left(\frac{\delta^2}{r}\frac{\partial^2\psi}{\partial z^2}-\frac{\partial}{\partial r}\left(\frac{1}{r}\frac{\partial\psi}{\partial r}\right)\right)+2\delta\frac{\partial}{\partial r}\left(\frac{1}{r}\frac{\partial\psi}{\partial z}\right)\frac{\partial}{\partial r}\left(\frac{1}{r}\frac{\partial\psi}{\partial r}\right)\right\},\end{aligned}\tag{8}$$

$$S_{\theta\theta}+\alpha\left\{\frac{\delta}{r}\frac{\partial(\psi,S_{\theta\theta})}{\partial(z,r)}-\frac{2\delta}{r^2}S_{\theta\theta}\frac{\partial\psi}{\partial z}\right\}=\frac{2\delta}{r^2}\frac{\partial\psi}{\partial z}+\beta\left\{\frac{2\delta^2}{r}\frac{\partial\left(\psi,\frac{1}{r^2}\frac{\partial^2\psi}{\partial z^2}\right)}{\partial(z,r)}-4\delta^2\left(\frac{\delta}{r^2}\frac{\partial\psi}{\partial z}\right)^2\right\},\tag{9}$$

$$S_{z\theta}+\alpha\left\{\frac{\delta}{r}\frac{\partial(\psi,S_{z\theta})}{\partial(z,r)}+\delta S_{z\theta}\frac{\partial}{\partial r}\left(\frac{1}{r}\frac{\partial\psi}{\partial z}\right)+S_{r\theta}\frac{\partial}{\partial r}\left(\frac{1}{r}\frac{\partial\psi}{\partial r}\right)\right\}=0,\tag{10}$$

$$\begin{aligned}&S_{zz}+\alpha\left\{\frac{\delta}{r}\frac{\partial(\psi,S_{zz})}{\partial(z,r)}+2S_{rz}\frac{\partial}{\partial r}\left(\frac{1}{r}\frac{\partial\psi}{\partial r}\right)+2\frac{\delta}{r}S_{zz}\frac{\partial^2\psi}{\partial r\partial z}\right\}=-2\frac{\delta}{r}\frac{\partial^2\psi}{\partial r\partial z}\\&+\beta\left\{-\frac{2\delta^2}{r}\frac{\partial\left(\psi,\frac{1}{r}\frac{\partial^2\psi}{\partial r\partial z}\right)}{\partial(z,r)}-\frac{4\delta^2}{r^2}\left(\frac{\partial^2\psi}{\partial r\partial z}\right)^2+2\frac{\partial}{\partial r}\left(\frac{1}{r}\frac{\partial\psi}{\partial r}\right)\left(\frac{\delta^2}{r}\frac{\partial^2\psi}{\partial z^2}-\frac{\partial}{\partial r}\left(\frac{1}{r}\frac{\partial\psi}{\partial r}\right)\right)\right\},\end{aligned}\tag{11}$$

where q is the modified pressure. Eliminating the modified pressure from (4) and (5), the compatibility equation in terms of stream function is obtained as

$$\begin{aligned}&\frac{\mathrm{Re}\,\delta}{r}\left\{\frac{\partial\left(\psi,\frac{\nabla^2\psi}{r}\right)}{\partial(z,r)}-\frac{\nabla^2\psi}{r^2}\frac{\partial\psi}{\partial z}\right\}=\frac{\delta}{r}\frac{\partial}{\partial z}\left(S_{rr}-S_{\theta\theta}\right)+\delta\frac{\partial^2}{\partial r\partial z}\left(S_{rr}-S_{zz}\right)\\&-\left(\frac{\partial^2}{\partial r^2}+\frac{1}{r}\frac{\partial}{\partial r}-\delta^2\frac{\partial^2}{\partial z^2}-\frac{1}{r^2}\right)S_{rz},\end{aligned}\tag{12}$$

The above mentioned modified pressure q and $\nabla^2\psi$ are defined as

$$q=p+\frac{\mathrm{Re}\,\delta}{2}\left\{\left(\frac{\delta}{r}\frac{\partial\psi}{\partial r}\right)^2+\left(\frac{1}{r}\frac{\partial\psi}{\partial r}\right)^2\right\}\quad\text{and}$$

$$\nabla^2\psi=\frac{\partial^2\psi}{\partial r^2}-\frac{1}{r}\frac{\partial\psi}{\partial r}-\delta^2\frac{\partial^2\psi}{\partial z^2}\tag{13}$$

and dimensionless parameters are

$$\alpha=\frac{\lambda_1 u_o}{R_o},\quad \alpha=\frac{\lambda_2 u_o}{R_o},\quad \delta=\frac{R_o}{l_o},\quad \mathrm{Re}=\frac{u_o R_o}{\nu},\quad \mathrm{f}=\frac{R(z)}{R_o},\quad \varepsilon=\frac{\lambda}{R_o},\tag{14}$$

where R(z) is the variable height of constriction and Re is the Reynolds number. Boundary conditions in terms of stream functions reduces as

$$\begin{aligned} &-\frac{1}{r}\frac{\partial\psi}{\partial r}=0, && \psi=-\frac{1}{2} && at && r=f,\\ &-\frac{\partial}{\partial r}\left(\frac{1}{r}\frac{\partial\psi}{\partial r}\right)=0, && \psi=0, && at && r=0. \end{aligned}\tag{15}$$

Now our task is to find the components of extra stress tensor and solve the above nonlinear equations along with the boundary conditions.

3. SOLUTION

Regular perturbation technique is applied to find the solution of non-linear equations by considering δ as a small parameter as follows

$$\psi=\psi_o+\delta\psi_1+\delta^2\psi_2+\cdots,$$

$$\begin{aligned} S_{rr} &= S_{rr}^{(0)}+\delta S_{rr}^{(1)}+\delta^2 S_{rr}^{(2)}+\cdots,\\ S_{r\theta} &= S_{r\theta}^{(0)}+\delta S_{r\theta}^{(1)}+\delta^2 S_{r\theta}^{(2)}+\cdots,\\ S_{rz} &= S_{rz}^{(0)}+\delta S_{rz}^{(1)}+\delta^2 S_{rz}^{(2)}+\cdots,\\ S_{\theta\theta} &= S_{\theta\theta}^{(0)}+\delta S_{\theta\theta}^{(1)}+\delta^2 S_{\theta\theta}^{(2)}+\cdots,\\ S_{\theta z} &= S_{\theta z}^{(0)}+\delta S_{\theta z}^{(1)}+\delta^2 S_{\theta z}^{(2)}+\cdots,\\ S_{zz} &= S_{zz}^{(0)}+\delta S_{zz}^{(1)}+\delta^2 S_{zz}^{(2)}+\cdots, \end{aligned}\tag{16}$$

Substituting equation(16) in equations (6)-(12) and (15) to find the systems of different orders.

3.1. Zeroth Order System and Solution:

Zeroth order system is obtained by comparing the coefficients of δ^0 on both sides of (6) - (12) and (15) andits solution is obtained of the form

$$S_{rr}^{(0)}=S_{r\theta}^{(0)}=S_{\theta\theta}^{(0)}=S_{\theta z}^{(0)}=0,\tag{17}$$

$$\psi_o=\frac{\eta^2}{2}\left(\eta^2-2\right),\ \text{where}\ \eta=\frac{r}{f}\tag{18}$$

once ψ_o is obtained then $S_{rz}^{(0)}$ and $S_{zz}^{(0)}$ are

$$S_{rz}^{(0)} = -\frac{4\eta}{f^3}, \qquad (19)$$

$$S_{zz}^{(0)} = -\frac{32\beta\eta^2}{f^6}, \qquad (20)$$

It is observed that ψ_o is independent of relaxation and retardation time parameters, which corresponds to Newtonian fluid. The normal stress $S_{zz}^{(0)}$ involves retardation time parameter.

3.2. First Order System and Solution:

First order system is found by equating the coefficients of δ on both sides of (6) - (12) and (15). The solution of these equations becomes as follows

$$S_{r\theta}^{(1)} = S_{\theta z}^{(1)} = 0, \qquad (21)$$

$$\psi_1 = \frac{\eta^2 f'}{36 f^3}\left(\eta^2 - 1\right)^2 \left\{\mathrm{Re} f^2\left(\eta^2 - 4\right) + 96\alpha\right\}, \qquad (22)$$

and then using (22) and (18), the first order stress components comes out of the form

$$S_{rr}^{(1)} = -\frac{4f'}{f^3}\left(3\eta^2 - 1\right), \qquad (23)$$

$$S_{\theta\theta}^{(1)} = -\frac{4f'}{f^3}\left(\eta^2 - 1\right), \qquad (24)$$

$$S_{rz}^{(1)} = -\frac{2\eta f'}{3f^8}\left\{16f^2\left(6\alpha\eta^2 - 3\mathrm{Re}\eta - 4\alpha + 3\mathrm{Re}\right) + \mathrm{Re} f^4\left(2\eta^4 - 6\eta^2 + 3\right) - 768\alpha\right\}, \qquad (25)$$

$$S_{zz}^{(1)} = -\frac{8f'}{3f^{11}}\left\{\begin{array}{l} 1536\alpha^2\eta^2 + 16\alpha\eta^2 f^2\left\{6\mathrm{Re}\left(\eta^2 - 1\right) - \alpha\left(12\eta^2 - 8\right) + 3\beta\left(\eta^2 + 1\right)\right\} \\ -2\mathrm{Re}\alpha\eta^2 f^4\left(2\eta^4 - 6\eta^2 + 3\right) - f^8\left(6\eta^2 - 3\right) \end{array}\right\}, \qquad (26)$$

The above solutions involve Oldroyd-B fluid parameters and reduces to Newtonian fluid by setting $\alpha = \beta = 0$.

3.2. Second Order System and Solution:

Second order system is obtained by comparing the coefficients of δ^2 on both sides of (6) - (12) and (15). The solution of second order system is obtained similarly as

$$\begin{aligned}\psi_2 = \frac{\eta^2\left(\eta^2-1\right)^2}{21600 f^8}[\ & f'^2 \{\ 5529600\alpha^2 + 4800\alpha f^2 (\eta^2(22\mathrm{Re}+73\alpha-181\beta)+(32\mathrm{Re}-90\alpha+152\beta) \\ & +40\mathrm{Re} f^4 \{\ 2\alpha(156\eta^4-568\eta^2+523)-3\beta(89\eta^4-342\eta^2+67)\ \}+\mathrm{Re}^2 f^6(\ 36\eta^6-314\eta^4+759\eta^2-818\ ) \\ & -18000 f^8\ \}+f^3 f''\{\ 4800\alpha(\ \eta^2(2\mathrm{Re}-9\alpha+21\beta)-(8\mathrm{Re}-10\alpha+20\beta)\ )-40\mathrm{Re} f^2\{\ 2\alpha(18\eta^4-74\eta^2+89) \\ & -9\beta(3\eta^4-14\eta^2+9)\ \}-3\mathrm{Re}^2 f^4(\ 2\eta^6-16\eta^4+14\eta^2-52\ )+3600 f^6\ \}\ ].\end{aligned} \tag{27}$$

$$\begin{aligned}S_{rr}^{(2)} = -\frac{1}{8f^6}[\ & 3f'^2\{\ 16(\ 3\beta(17\eta^4-18\eta^2+5)+\alpha(39\eta^4-30\eta^2-5)\ )+\mathrm{Re} f^2(\ 21\eta^6-70\eta^4+45\eta^2-4\ )\ \} \\ & -ff''(\eta^2-1)\{48(\ \alpha(7\eta^2+1)+3\beta(\eta^2-1)\ )+\mathrm{Re} f^2(7\eta^4-23\eta^2+4)\ \}\ ],\end{aligned} \tag{28}$$

$$\begin{aligned}S_{\theta\theta}^{(2)} = -\frac{(\eta^2-1)}{8f^6}[\ & 3f'^2\{\ 16(\ 15\beta(\eta^2-1)+\alpha(3\eta^2+5)\ )+\mathrm{Re} f^2(\ 3\eta^4-11\eta^2+4\ )\ \} \\ & +ff''(\eta^2-1)\{48(\ \alpha-3\beta\ )+\mathrm{Re} f^2(\eta^2-4)\ \}\ ],\end{aligned} \tag{29}$$

$$\begin{aligned}S_{rz}^{(2)} = \frac{\eta^2\left(\eta^2-1\right)^2}{21600 f^8}[\ & f'^2 \{\ 5529600\alpha^2 + 4800\alpha f^2 (\eta^2(22\mathrm{Re}+73\alpha-181\beta)+(32\mathrm{Re}-90\alpha+152\beta) \\ & +40\mathrm{Re} f^4 \{\ 2\alpha(156\eta^4-568\eta^2+523)-3\beta(89\eta^4-342\eta^2+67)\ \}+\mathrm{Re}^2 f^6(\ 36\eta^6-314\eta^4+759\eta^2-818) \\ & -18000 f^8\ \}+f^3 f''\{\ 4800\alpha(\ \eta^2(2\mathrm{Re}-9\alpha+21\beta)-(8\mathrm{Re}-10\alpha+20\beta)\ )-40\mathrm{Re} f^2\{\ 2\alpha(18\eta^4-74\eta^2+89) \\ & -9\beta(3\eta^4-14\eta^2+9)\ \}-3\mathrm{Re}^2 f^4(\ 2\eta^6-16\eta^4+14\eta^2-52\ )+3600 f^6\ \}\ ].\end{aligned} \tag{30}$$

* * *

$$\begin{aligned}S_{zz}^{(2)} = -\frac{2}{135 f^{14}}[\ & f'^2\{\ -368640\alpha^3\eta^2(12\eta^2-19)+960\alpha^2\eta^2 f^2(6\mathrm{Re}(6\eta^4-26\eta^2+3)+\alpha(120\eta^4-168\eta^2+25) \\ & +3\beta(290\eta^4-450\eta^2+270)\ )+24\mathrm{Re}\,\alpha\eta^2 f^4(\ 120\mathrm{Re}(\ 2\eta^6-8\eta^4+9\eta^2-3\ )-2\alpha(\ 585\eta^6-1960\eta^4+2010\eta^2 \\ & -618\ )+\beta(\ 1205\eta^6-4270\eta^4+3765\eta^2-926\ )+\mathrm{Re}^2\eta^2 f^6(\ 60\beta(2\eta^4-6\eta^2+3)^2+\alpha(\ -354\eta^8+2220\eta^6 \\ & -4590\eta^4+3765\eta^2-1019\ )-360 f^8(\ \alpha(39\eta^4-48\eta^2+13)-3\beta(5\eta^4-4\eta^2+1)\ )-45\mathrm{Re} f^{10}(\ 6\eta^6-21\eta^4+ \\ & 15\eta^2-2\ )\ \}+3ff''\{\ 368640\alpha^3\eta^2(\eta^2-1)-320\alpha^2\eta^2 f^2(-6\mathrm{Re}(10\eta^4-18\eta^2+9)+\alpha(120\eta^4-168\eta^2+49) \\ & +\beta(54\eta^4-138\eta^2+85)\ )-8\mathrm{Re}\,\alpha\eta^2 f^4(\ 2\alpha(\ 15\eta^6-80\eta^4+60\eta^2-6\ )+3\beta(\ 15\eta^6-70\eta^4+75\eta^2-22\ )\ ) \\ & +\alpha\mathrm{Re}^2\eta^2 f^6(\ 6\eta^8-40\eta^6+90\eta^4-90\eta^2+29\ )-120 f^8(\ \alpha(9\eta^4-8\eta^2+1)-3\beta(3\eta^4-4\eta^2+1)\ )+ \\ & 5\mathrm{Re} f^{10}(\ 2\eta^6-9\eta^4+9\eta^2-2\ )\ \}\ ]\end{aligned} \tag{31}$$

Which are general solutions and reduces to viscous solution by setting $\alpha = \beta = 0$, Jeffrey fluid by setting $\alpha = 0$ and Maxwell fluid by setting $\beta = 0$.

The velocity components u and w could be obtained by making use of ψ_o, ψ_1, ψ_2 in (16).

3.4. Pressure Distribution:

Eliminating the modified pressure q from equations (4) - (5) and then substituting the perturb form of pressure as

$$p = p_o + \delta\, p_1 + \delta^2 p_2 + \cdots, \qquad (32)$$

in equations (4) - (5). Now equating the coefficients of different powers of δ on both sides of (4) - (5). To solve these systems apply

$$p = \int_0^z \frac{\partial p}{\partial z}dz + \int_0^r \frac{\partial p}{\partial r}dr, \qquad (33)$$

to the different orders for pressure. Solution of zeroth order pressure is

$$\begin{aligned} p_o &= \frac{1}{4\pi}\left(5\varepsilon^3 - 18\varepsilon^2 + 24\varepsilon - 16\right)\tanh^{-1}\left(\frac{\tan 2\pi z}{\sqrt{\varepsilon - 1}}\right) \\ &+ \frac{\varepsilon \sin 2\pi z}{24\pi f(\varepsilon - 1)}\left\{\frac{8}{f^2} + \frac{10(\varepsilon - 2)}{f(\varepsilon - 1)} + \frac{15\varepsilon^2 - 44\varepsilon + 44}{(\varepsilon - 1)^2}\right\}. \end{aligned} \qquad (34)$$

It is observed that zeroth order pressure is independent of relaxation and retardation time parameters and similar to viscous solution.

Solution of first order pressure is obtained of the form

$$\begin{aligned} p_1 &= 16\left(8\alpha + r^2(\mathrm{Re} - 2\alpha + 2\beta)\right)\left(\frac{1}{(\varepsilon - 1)^8} - \frac{1}{f^8}\right) \\ &- \frac{32}{9}(3\,\mathrm{Re} - 4\alpha)\left(\frac{1}{(\varepsilon - 1)^6} - \frac{1}{f^6}\right) + \mathrm{Re}\left(\frac{1}{(\varepsilon - 1)^4} - \frac{1}{f^4}\right), \end{aligned} \qquad (35)$$

which involves the relaxation and retardation time parameters. It is observed that the first order pressure for viscous case could be found by setting $\alpha = \beta = 0$.

The solution of second order pressure in integral form is obtained as follows

$$\begin{aligned} p_2 &= -\frac{8r^2 f'}{f^5} + \frac{1}{270}\int_0^z \Big[\, \{\, 6082560\alpha^2 + 960\alpha(41\alpha + 191\beta - 138\mathrm{Re})f^2 - 144\mathrm{Re}(49\alpha - 9\beta)f^4 \\ &+ (10800r^2 + 121\mathrm{Re}^2)f^6 - 3960 f^8 \,\}f'^2 - 3f\{\, 184320\alpha^2 + 320\alpha(\alpha + 31\beta - 18\mathrm{Re})f^2 - 48\mathrm{Re}(7\alpha + \beta)f^4 \\ &+ (720r^2 + 11\mathrm{Re}^2)f^6 - 120 f^8 \,\}f'' \,\Big]dz \end{aligned} \qquad (36)$$

It is observed that the second order pressure is more general and one can obtained the second order pressure for Jeffrey fluid by setting $\alpha = 0$, Maxwell fluid by setting $\beta = 0$, Newtonian fluid by setting $\alpha = \beta = 0$.

Wall shear stress up to second order is obtained of the form

$$\begin{aligned} \tau_\omega &= -\frac{4}{f^3} + \frac{2\delta f'}{3f^8}\left(\mathrm{Re}\, f^4 + \alpha(768 - 32f^2)\right) + \frac{\delta^2}{540 f^{11}}\Big[\, f'^2\{\, 960\alpha f^2(137\alpha - 163\beta - 54\,\mathrm{Re}) - 1105920\alpha^2 \\ &- 48\,\mathrm{Re}\, f^4(157\alpha - 27\beta) + 67\,\mathrm{Re}^2 f^6 + 5760 f^8 \,\} - 3f^3 f''\{\, 320\alpha(\alpha + \beta - 6\,\mathrm{Re}) - 16\,\mathrm{Re}\, f^2(11\alpha + 3\beta) \\ &+ 5\,\mathrm{Re}^2 f^4 + 240 f^6 \,\}\,\Big] \end{aligned} \qquad (37)$$

The points of separation and reattachment are given by $\tau_{\omega} = 0$, the resulting equation is quadratic in Re and the solution in terms of Re is

$$\mathrm{Re} = \frac{-b \pm \sqrt{b^2 - 4ac}}{2a}, \tag{38}$$

where

$$a = \delta^2 f^6 \left(15 ff'' - 67 f'^2\right), \tag{39}$$

$$b = 24\delta f^2 \{ \; 15 f^5 f' - 2160\delta f'^2 - 2\delta\left(15\alpha - 27\beta\right) f^2 f'^2 + 240\alpha\delta f f'' + 2\delta\left(11\alpha + 3\beta\right) f^3 f'' \; \}, \tag{41}$$

$$c = 240\{ \; 48\delta\alpha f^5 f' + 4608\alpha^2\delta^2 f'^2 - 4\alpha\delta^2\left(137\alpha - 163\beta\right) f^2 f'^2 + f^8\left(9 - 24\delta^2 f'^2\right) + 3\delta^2 f^9 f'' \\ - 4\delta\alpha f^3\left(288 f' - \delta\left(\alpha + \beta\right) f''\right) \; \}. \tag{42}$$

Equation (38) gives the separation and reattachment points.

4. GRAPHICAL DISCUSSION

In this section, solutions are presented graphically by using different values of the parameters for the stream lines, wall shear stress, zero wall shear stress, pressure gradient and velocity profile. Solutions are analyzed numerically for the relaxation time (α), retardation time (β), height of constriction (ε) and Reynolds number (Re).

In these figures z- axis lies in the horizontal direction and r- axis is perpendicular to it. The zeroth order solution corresponds to laminar flow and behavior is similar to Newtonian fluid. First order solution induces the clockwise and counterclockwise rotational motion in the converging and diverging regions, which indicates the separation point in the converging region and reattachment point in the diverging region. Figure 2(c) shows the behavior of stream lines for second order solution which also shows the rotational motion which indicates the separation and reattachment region. Figure 2(d) presents the stream line solution up to second order. It is observed that by setting $\alpha = 0, \; \beta = 0$, the stream lines are similar to [6].

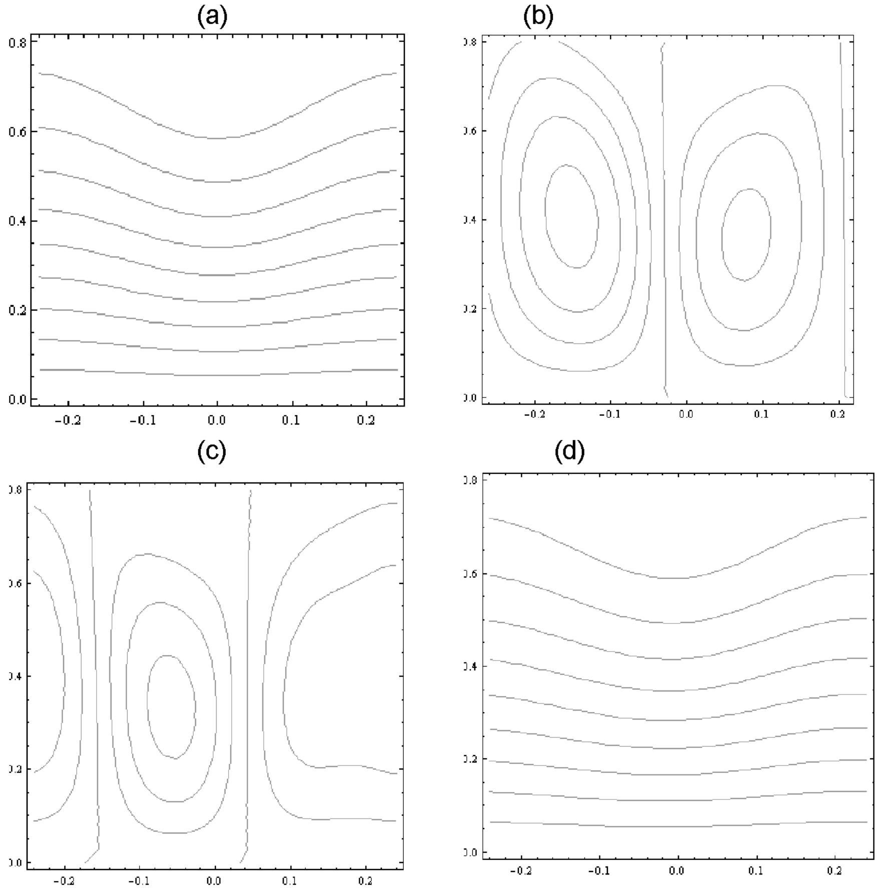

Fig.2. The behavior of stream lines for zeroth order 2(a), first order 2(b), second order 2(c) and up to second order 2(d) presented for

$$\mathrm{Re} = 12,\ \varepsilon = 0.2,\ \delta = 0.1,\ \alpha = 0.04,\ \beta = 0.2.$$

In these figures z- axis lies in the horizontal direction and r- axis is perpendicular to it. The zeroth order solution corresponds to laminar flow and behavior is similar to Newtonian fluid. First order solution induces the clockwise and counterclockwise rotational motion in the converging and diverging regions, which indicates the separation point in the converging region and reattachment point in the diverging region. Figure 2(c) shows the behavior of stream lines for second order solution which also shows the rotational motion which indicates the separation and reattachment region. Figure 2(d) presents the stream line solution up to second order. It is observed that by setting $\alpha = 0,\ \beta = 0$, the stream lines are similar to [6].

Figure 3 predicts the behavior of α on wall shear stress in the converging and diverging sections of the artery for the fixed values of $\mathrm{Re},\ \varepsilon,\ \delta,\ \beta$. Wall shear stress increases near the throat of the artery as α increases. Wall shear stress decreases due to reverse flow in the converging and diverging sections of the artery.

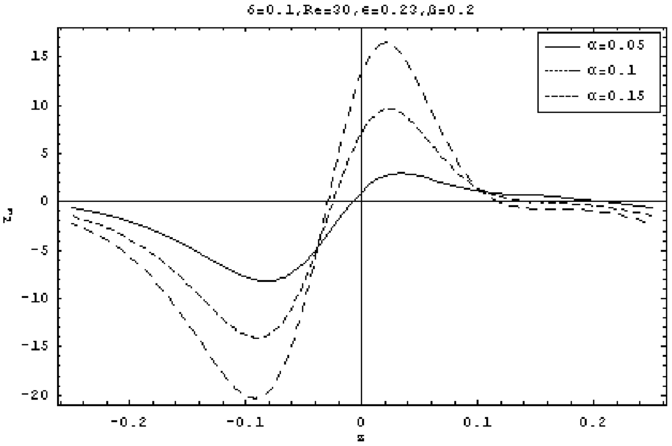

Fig.3. Effect of α on wall shear stress.

In figure 4, zero wall shear stress is plotted for α having fixed values of β and ε in the converging section of the artery. The purpose of investigation is to determine the critical value of Re at which separation occurred in the converging region of the artery. As the critical Re reached the separation occurs in the converging region of the artery.

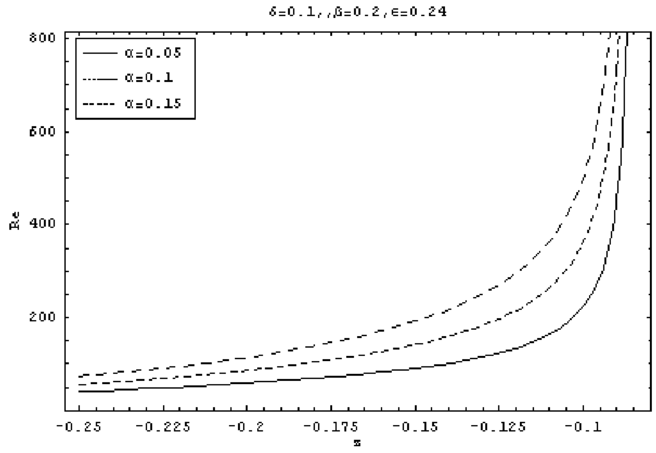

Fig.4. Separation point for α in converging region.

In figure 5, zero wall shear stress is presented for α with fixed values of β and ε in diverging section of the artery. The purpose of investigation is to determine the critical value of Re at which separation occurred in the diverging region of the artery. When the critical Re reached the reattachment occurs in the diverging region of the artery. We observe form figure 5 that as we increase α the critical Re decreases.

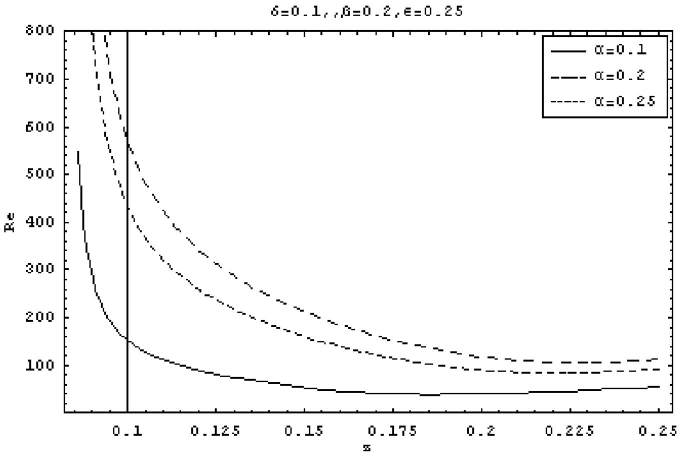

Fig.5. Reattachment point for α in the diverging region.

In figure 6, the effect of α over the axial velocity of the blood is plotted. As the value of α increases axial velocity decreases in the converging section of the artery and becomes maximum over the constriction and becomes negative diverging section of the artery, which predicts the back flow in the converging and diverging region of the artery, which indicates the separation points in the converging region and reattachment points in the diverging region of the artery.

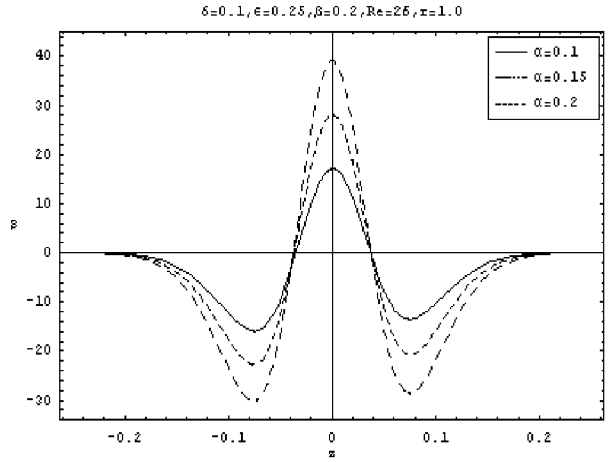

Fig.6. Velocity distribution for α .

Figure 7 presents the distribution of pressure gradient for α, by increasing α pressure gradient decreases on the constricted region and obtain parabolic shape. Reverse flow indicates the negative pressure gradient in the converging as well as in diverging section of the artery.

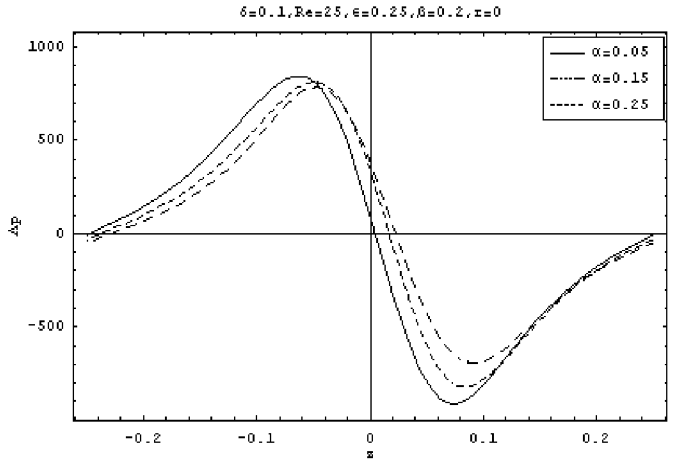

Fig.7. Pressure gradient for α .

5. DEDUCTIONS

The present investigation for Oldroyd-B is more general and we can obtain the results for

(i) Newtonian fluids by substituting λ_1, λ_2 equal to zero.

(ii) Maxwell fluid by substituting λ_2 equal to zero.

(iii) Jeffrey fluid by substituting λ_1 equal to zero.

(iv) Second grade fluid by substituting $\lambda_1 = 0$, $\mu\lambda_2 = \alpha_1$.

6. CONCLUSIONS

In this article we analyze the Oldroyd-B fluid for velocity component, pressure gradient, wall shear stress, separation points and draw the graphs for each. From the graphical representation we observe that the solution obtained in this analysis are very near to the physical significance of the parameters involved in this study. The general patron of streamlines is same as in [4, 5], by setting λ_1, λ_2 equal to zero, the wall shear stress is similar as [2, 3] and separation and reattachment points are similar with [3]. We observe the following

(i) As the Re increases wall shear stress and pressure gradient increases.

(ii) By the increase in ε increases the wall shear stress and pressure gradient.

(iii) Critical Re decreases by the increase in ε.

(iv) Increase in α increases in pressure, velocity and wall shear stress.

(v) Critical Re decrease by the increase of α in the converging and diverging region.

REFERENCES

1. D. F. Young, J. Engg. Int., Trans. Am. Soc. Mech. Engrs., 90 (1968), 248.
2. J. H. Forrester and D.F. Young, J. Biomech., 3 (1970) 297.
3. B. E. Morgan and D. F. Young, J. Math. Biol., 36 (1974) 39.
4. K. Haldar, Archives of Mechanics, 43 (1) (1991) 107.
5. J. C. F. Chow and K. Soda, Physics of Fluids, 15 (10) (1972) 1700.
6. J. B. Shukla, R. S. Parihar and B. R. P. Rao, Bull. of Math. Bio., 42 (1980) 283.
7. J. C. Mishra and G. C. Shit, Int. J. of Eng. Sci., 44 (2006) 662.
8. K. Haldar, Bull. of Math. Bio., 47 (4) (1985) 545.
9. C. Tu and M. Deville, J. Biomech., 29 (7) (1996) 899.